Atmospheric
Chemistry
and Physics

Observing convective activities in complex convective organizations and their contributions to precipitation and anvil cloud amounts

Zhenquan Wang and Jian Yuan

School of Atmospheric Sciences, Nanjing University, Nanjing, China

Correspondence: Zhenquan Wang (zhqwang@smail.nju.edu.cn)

Abstract. The convective processes of precipitation and the production of anvil clouds determine the Earth's water and radiative budgets. However, convection could have very complicated convective organizations and behaviors in the tropics. Many convective activities in various life stages are clustered and connected in complex convective organizations, and distinguishing their behaviors is difficult. In this work, based on hourly infrared brightness temperature (BT) satellite images, with a novel variable-BT tracking algorithm, complex convective organizations are partitioned into organization segments of single cold-core structures as tracking targets. The detailed evolution of the organization structures (e.g., the variation in the cold-core BT, mergers and splits of cold cores) can be tracked, and precipitation and anvil clouds are explicitly associated with unique cold cores. Compared with previous tracking algorithms that focused only on variations in areas, the novel variable-BT tracking algorithm is designed to track the core structure in complex convective organizations and document the evolution of both the area and BT structures. For validation, the tracked motions are compared against the radiosonde cloud-top winds, with a mean speed difference of $-1.6\,\mathrm{m\,s^{-1}}$ and a mean angle difference of $0.5°$.

With the novel variable-BT tracking algorithm, the behaviors of oceanic convection over the tropical western Pacific Ocean are investigated. The results show that the duration, precipitation and anvil amount of lifetime accumulation all have simple loglinear relationships with the cold-core-peak BT. The organization segments of the peak BT values less than $220\,\mathrm{K}$ are long-lived, with average durations of 4–16 h, whereas the organization segments of the warmer-peak BT values disappear rapidly within a few hours but with a high occurrence frequency. The decay process after the cold-core peak contributes to more precipitation and anvil clouds than the development process does. With the core peaking at a colder BT, the differences in the accumulated duration, precipitation and anvil production between the development and decay stages increase exponentially. Additionally, the occurrence frequency of mergers and splits also has a loglinear relationship with the cold-core-peak BT. For the life cycles of the same cold-core-peak BT, the lifetime-accumulated precipitation and anvil amount are strongly enhanced in complicated life cycles with the occurrence of mergers and splits, compared with those with no mergers or splits. For the total tropical convective cloud water budget, long-lived complicated life cycles make the largest contribution to precipitation, whereas long-lived complicated and short-lived simple life cycles make comparable contributions to the anvil cloud amount and are both important.

1 Introduction

Precipitation and anvil clouds are two key components of the convective cloud water budget but are usually accompanied by very complicated microphysical and dynamic processes. In climate models, their representations are determined by tunable parameters with large uncertainties, e.g., precipitation and detrainment efficiency (Rennó et al., 1994; Zhao, 2014; Clement and Soden, 2005; Zhao et al., 2016; Suzuki et al., 2013). In cloud-resolving models, the parameterization scheme of convection is still subject to many uncertainties in ice cloud microphysics and subgrid turbulence (Matsui et al., 2009; Blossey et al., 2007; Powell et al., 2012; Bretherton, 2015; Atlas et al., 2024), although cloud dynamics and microphysics can be resolved at fine scales. The challenge is partially because the detailed convection processes of precipitation and the production of anvil clouds have not been sufficiently explored from observations to advance understanding and model parameterization.

The spatial organization of convection varies from a simple isolated cell to a complicated structure that consists of many convective activities in various life stages. The variation in convection organization is closely related to changes in precipitation and the production of anvil clouds (Yuan and Houze, 2010; Yuan et al., 2011; Tobin et al., 2012; Wing and Emanuel, 2014; Mauritsen and Stevens, 2015; Ruppert and Hohenegger, 2018; Bony et al., 2020; Bao and Sherwood, 2019; Houze, 2004). Cloud-resolving models and observations both suggest that convective organizations are important bridges for the interactions between convection and the environment (Tobin et al., 2012; Blossey et al., 2005; Coppin and Bony, 2015; Wing and Emanuel, 2014; Wing et al., 2017; Holloway et al., 2017; Muller and Bony, 2015; Sokol and Hartmann, 2022). Through radiative feedback and circulation, convective organizations are associated with the nonconvecting environment. The drier free troposphere and enhanced radiative cooling of nonconvecting regions can reinforce subsidence to expand the dry region and thereby force the convection in the moist region to aggregate (Blossey et al., 2005; Coppin and Bony, 2015). Over warm oceans, stronger mass convergence and surface turbulent fluxes promote aggregation by developing deep convection and inhibiting scattered convective activities (Coppin and Bony, 2015; Holloway et al., 2017; Wing et al., 2017). Although organizational variations of convection can influence precipitation efficiency (Bao and Sherwood, 2019), when the total atmospheric water amount is not known and is difficult to measure, increased precipitation efficiency might not guarantee a decrease in the anvil cloud amount. Thus, the links among convective organizations, precipitation and anvil clouds still need further observational evidence as constraints for understanding their climate feedback processes.

However, observing the organization and behavior of convection is still challenging. Although active radar and lidar sensors on polar-orbit satellites and ground-based observa-

tories can penetrate convective clouds, their spatiotemporal sampling is too sparse for tracking convection behaviors, without a full picture of the spatial organization of convection. From the images of the brightness temperature at $10.8\,\mu m$ (BT_{11}) of geostationary satellites (GEOs), pixels of thin cirrus clouds cannot be accurately distinguished from cloudless pixels, but the major structure of the organized convection, consisting of the deep convective clouds and their associated anvil clouds, can be observed continuously in time and used for tracking (Richards and Arkin, 1981; Hendon and Woodberry, 1993; Fu et al., 1990). For identifying convection from GEO images, two methods have been proposed in previous studies. One method is to identify the contiguous area under a fixed BT_{11} threshold (Goyens et al., 2011; Schröder et al., 2009; Huang et al., 2018; Williams and Houze, 1987; Chen and Houze, 1997; Kolios and Feidas, 2009; Laing et al., 2008; Feidas and Cartalis, 2007; Fu et al., 2023; Yang et al., 2020; Tsakraklides and Evans, 2003). Based on the fixed threshold, the identified targets usually have complex organizations, but the fixed-threshold method is not capable of being used to further distinguish the detailed convective activities inside complex organizations. In addition, variable-BT_{11} identification has been proposed in recent years, in which a set of adaptive BT_{11} thresholds are used to divide the clustered convection complex into independent convective systems for tracking (Yuan and Houze, 2010; Fiolleau and Roca, 2013; Feng et al., 2023; de Laat et al., 2017; Bouniol et al., 2016; Heikenfeld et al., 2019; Zinner et al., 2008, 2013). This approach makes it possible to track the detailed variations in complex convection organizations, particularly with respect to tracking the evolution of the BT_{11} structures.

Convective systems can merge and split, and their BT_{11} structures can change rapidly. These complicated behaviors make them difficult to track. Most multiple-target tracking algorithms (e.g., multiple-hypothesis tracking) rarely consider mergers and splits and can only be used to track the targets whose number is invariant or merely varies with birth and death events (Blackman, 2004). The aim of storm tracking is to find the associations among convective systems at different times. The most widely used storm-tracking method is based on the overlap in areas between two targets at different times (Williams and Houze, 1987). If convective systems of different times overlap with each other sufficiently, they are associated in time and are deemed to be one storm at different times. This method permits mergers and splits but has flaws in tracking fast-moving storms (Huang et al., 2018). On the other hand, storm positions can be well predicted by matching the BT_{11} patterns in the latter image via cross-correlation (Leese et al., 1971; Nieman et al., 1997; Velden et al., 1998; Salonen and Bormann, 2016; Hersbach et al., 2020). This method has been widely applied to atmospheric motion vector observations (Salonen and Bormann, 2016), which are among the most important data sources for assimilation into reanalysis winds (Hersbach et al., 2020). However, the asso-

ciation of convective systems at different times is difficult to determine by their positions when they merge and split. Nevertheless, these two methods are complementary and can be combined to first derive storm displacements and then determine the temporal associations between convective systems according to the dynamic overlap (i.e., the overlap in areas after moving it to the position predicted by cross-correlation) (Feng et al., 2023; Zinner et al., 2013).

In this work, complex convective organizations (CCOs) are segmented into simple structural components of single cold cores and tracked separately on the basis of a novel variable-BT_{11} tracking algorithm. Compared with fixed-threshold tracking, variable-BT_{11} tracking has the advantages of documenting more detailed convective evolution in CCOs. Although several variable-BT_{11} tracking algorithms have been proposed, the tracked life cycle is still described mostly by the variation in areas and lacks BT_{11} structural information. *This novel variable-BT_{11} tracking algorithm developed in this work has the capability of tracking the BT_{11} structural evolution in CCOs.* The precipitation and non-precipitating anvil clouds in CCOs are explicitly associated with unique cold cores with a well-organized structure in the novel tracking algorithm.

This paper is laid out as follows. Section 2 describes the data and methods used in our analyses. Section 3 introduces the novel variable-BT_{11} segment tracking algorithm and its comparison to fixed-threshold tracking. Section 4 explores the relationships of the convection duration, precipitation and anvil production with the BT_{11} structures. Section 5 presents conclusions.

2 Data and methods

2.1 Images from GEOs

The BT_{11} images in the tropics between 20° S–20° N and 90° W–170° E were taken by radiometer imagers on geostationary Multi-functional Transport Satellite 1 Replacement and 2 Replacement (MTSAT-1R and MTSAT-2R), with a scanning start time of half an hour and view zenith angles of less than 60°. The data of those BT_{11} images from 2006 with 1 h and 8 km resolutions were obtained from the Satellite ClOud and Radiative Property retrieval System (SatCORPS) of the Clouds and the Earth's Radiant Energy System (CERES) project. In the CERES SatCORPS, the BT_{11} was calibrated against the Moderate Resolution Imaging Spectroradiometer (MODIS) from Aqua (Doelling et al., 2013, 2016). To facilitate data processing, the BT_{11} images of 8 km pixels were further gridded to 0.05° via linear interpolation (Amidror, 2002).

2.2 Global precipitation measurement (GPM)

At fine scales (0.1° and half-hour resolution), the GPM data combine all available sensors for precipitation estimates,

which include microwave imagers from multiple low-Earth orbit satellites, the infrared (IR) channel of GEO radiometers and land-surface rain gauges (Huffman et al., 2007, 1997). The microwave brightness temperature is sensitive to atmospheric hydrometers of precipitation but has sparse spatiotemporal sampling due to its sun-synchronous orbit. For those grids without microwave observations, the GEO-IR BT_{11} was used to estimate precipitation according to the spatially varying calibration coefficient of the microwave precipitation rates (Huffman et al., 1997). To improve accuracy, rain gauges were further used to rescale satellite estimates of precipitation rates (Huffman et al., 1997). It has been demonstrated that this satellite-based precipitation product performs well for strong precipitation events with a mean bias smaller than $1\,\mathrm{mm\,d^{-1}}$ but misses 20 %–80 % of the light precipitation ($< 10\,\mathrm{mm\,d^{-1}}$) (Tian et al., 2009). In the tropics, light precipitation ($< 1\,\mathrm{mm\,h^{-1}}$) accounts for approximately 55 %–70 % of the precipitation area but contributes to only 9 %–18 % of the total precipitation (Yuan and Houze, 2010). In this work, only precipitation rates greater than $1\,\mathrm{mm\,h^{-1}}$ are considered the regions with precipitation, since light precipitation has high uncertainty in the GPM data and relatively low contributions to total precipitation.

2.3 Cloud-top winds from ground-based radar and radiosonde observations

Cloud detection from radar and wind observations from radiosondes were combined to derive cloud-top winds at three tropical ground-based observatories of the Atmospheric Radiation Measurement (ARM) program: Darwin (12.4° S, 130.9° E), Manus Island (2.1° S, 147.4° E) and Nauru Island (0.5° S, 166.9° E). The vertical distribution of hydrometers up to 20 km above the ground was detected via 35 GHz millimeter-wave cloud radar (MMCR), with temporal and spatial resolutions of 10 s and 45 m, respectively. The best-estimate reflectivity of the MMCR in the range of −50 to 20 dBZ was provided in the ARM program Active Remote Sensing of Clouds (ARSCL) value-added product at the three sites. A reflectivity higher than −40 dBZ was identified as a cloud (Zhao et al., 2017). To match the GEO observations, instantaneous cloud profiles within 5 min around the scanning time of the GEO radiometer imager at these three sites were collected to compute the cloud fraction. The 10 min cloud-fraction profile was computed as the ratio of the number of cloud occurrences to the total number of observations at each height. Continuous levels of cloud fraction greater than zero were identified as cloud layers. The thickest high cloud layer with a top greater than 5 km and a maximum cloud fraction of at least 50 % was selected as the major high cloud layer passing over the sites. The cloud top refers to the uppermost height of the major high cloud layer.

Winds were detected by the ARM balloon-borne radiosondes with high vertical and temporal resolutions of 10 m and 2.5 s, respectively. The accuracy of the radiosonde wind

speed was approximately $0.5\,\mathrm{m\,s^{-1}}$. The radiosondes were launched two times a day at Manus and Nauru (approximately 11:30 and 23:30 UTC) and four times a day at Darwin (approximately 04:30, 11:15, 16:30 and 23:15 UTC). Notably, balloon-borne radiosondes usually take hours and drift dozens of kilometers away from the launch location to approach the cloud-top height. To derive cloud-top winds, the time difference between the balloon-borne radiosondes reaching the cloud-top height and the MMCR observations of the cloud top must be within 1 h for quality control.

2.4 Comparison of cloud-top winds and tracked cloud motions

The difference between the observed cloud-top winds and the tracked cloud motions is assessed as follows, which is consistent with those in Nieman et al. (1997):

$$\text{speed bias} = \frac{1}{N}\sum_{i=1}^{N}\left(\sqrt{U_i^2 + V_i^2} - \sqrt{U_r^2 + V_r^2}\right), \quad (1)$$

$$\text{angle bias} = \frac{1}{N}\sum_{i=1}^{N}\left(\arctan\left(\frac{V_i}{U_i}\right) - \arctan\left(\frac{V_r}{U_r}\right)\right), \quad (2)$$

$$\text{MVD} = \frac{1}{N}\sum_{i=1}^{N}\sqrt{(U_i - U_r)^2 + (V_i - V_r)^2}, \quad (3)$$

$$\text{SD} = \sqrt{\frac{1}{N}\sum_{i=1}^{N}\left(\sqrt{(U_i - U_r)^2 + (V_i - V_r)^2} - \text{MVD}\right)^2}, \quad (4)$$

$$\text{RMSE} = \sqrt{\text{MVD}^2 + \text{SD}^2}. \quad (5)$$

Here, the mean speed and angle bias, the mean vector difference (MVD), the standard deviation (SD) of the MVD, and the root-mean-square error (RMSE) of the tracked cloud motions compared with the observational cloud-top winds were computed. U and V are the x- and y-component winds, respectively. The subscripts i and r indicate an individual sample of the tracked cloud motion and the corresponding reference cloud-top winds of radiosondes, respectively, and N is the total number of samples.

2.5 The t test and confidence intervals

The 95 % confidence interval for the mean value was computed via the t test: $\overline{x} \pm t_c \frac{s}{\sqrt{N}}$, where $\overline{x}$ is the mean value of all samples, t_c is the critical value for t and s is the standard deviation of all the samples. N is the number of independent samples, and N is determined by the sample length divided by the distance between independent samples (Bretherton et al., 1999).

3 Tracking the convective organization segments

To distinguish clustered convective activities in CCOs, the organization segments (OSs) of single but variable-BT_{11} cold cores are partitioned from CCOs (Fig. 1a) and are tracked by combining the cross-correlation and the area overlap

(Fig. 1b) on the basis of the hourly infrared satellite images. This novel variable-BT_{11} segment tracking algorithm and its difference from the conventional fixed-threshold tracking algorithm are introduced in this section as follows.

3.1 Segmenting CCOs into the OSs of single cold cores

As illustrated in Fig. 1a, the CCO is the complex organization of multiple connected convections and is identified by the contiguous area of the BT_{11} colder than 260 K. The 260 K threshold of BT_{11} is normally used to identify the pixels with high clouds (Minnis et al., 2008, 2011). The 260 K isotherm can enclose 95 % of deep convective clouds and as much of the anvil cloud as possible but with the least contamination from lower-level clouds (Yuan and Houze, 2010; Yuan et al., 2011; Chen and Houze, 1997). To identify the organized structures of CCOs, a set of adaptively variable-BT_{11} thresholds from 180–260 K per 5 K interval and a minimum area threshold of $1000\,\mathrm{km^2}$ are used to capture the "growth rings" in CCOs. As shown in Fig. 1a, these rings reflect the CCO structure in three dimensions, namely x, y and BT_{11}, and are the fundamental indicators of its internal dynamics (Houze, 2004). The innermost ring of the coldest local BT_{11} is defined as the cold core, which is the most active vertically developing region. The BT_{11} of the cold core represents the depth at which the convection developed. For a CCO consisting of multiple cold cores, the BT_{11} of the coldest core in the CCO is defined as the CCO BT_{11} for representing the depth of CCO development. The isolated ring of the warmest BT_{11} that encloses only one cold core is the cold center. The convection would be connected (disconnected) to the surrounding convections outside (inside) the center. Thus, the cold-center BT_{11} can be used to indicate the connecting condition between the convections in the CCO.

The segmented single-core structural component of CCOs is defined as the OS, as illustrated in Fig. 1a. To partition the CCO into OSs, the pixels lying outside the centers are assigned to the connected neighborhood OSs by the 1 K interval. To be specific, all BT_{11} contours of the 1 K interval between the cold-center BT_{11} and 260 K need to be found first. The assignment of the pixels outside the centers is conducted in the order from cold to warm BT_{11} contours of the 1 K interval. The initial OS is just the center, and it is updated after every 1 K interval assignment. An example illustration of the 1 K interval assignment is shown in Fig. 2. On the basis of the eight-point-connected neighborhood in which the eight surrounding points are recognized as the neighborhood connected to the center point, the distance between 2 target pixels is computed as the number of necessary pixels connecting them. According to the nearest linear distance, as shown in Fig. 2a, some of the pixels assigned to OS2 (light-green pixels in Fig. 2a) are disconnected from OS2 but connected to OS1. After the assignment, OS2 is composed of two disconnected parts. For an organized convective system, the assigned pixels outside the center can also be un-
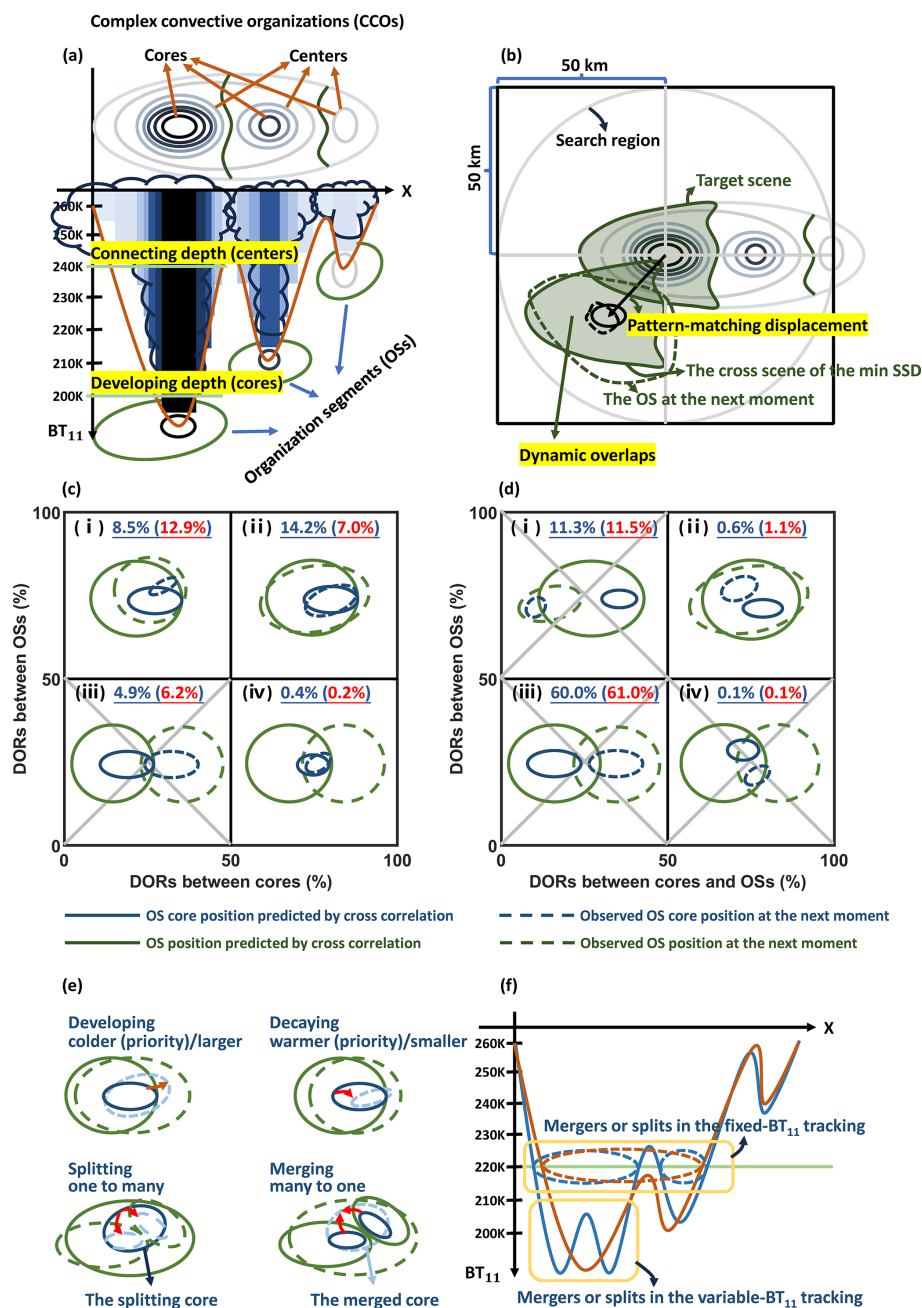
Figure 1. Schematic illustrations of the variable-BT_{11} segment tracking algorithm. **(a)** Example illustrations of segmenting the CCO into single-core OSs as tracking targets. The CCO 3-dimensional structures in x, y and BT_{11} are identified by the adaptive variable-BT_{11} thresholds. The cold-core BT_{11} indicates the depth of development. The cold-center BT_{11} indicates the depth of the connection. **(b)** Example illustrations of tracking the OS by combining cross-correlation and overlap in areas. The OS is moved to the position predicted by cross-correlation and then overlaps with the OSs at the next moment. **(c–d)** Dynamic overlapping situations of two OSs of different moments when their cores have overlaps and no overlaps, respectively. The solid blue and green lines indicate the core and OS of the current moment at the position predicted by cross-correlation, respectively. The dashed blue and green lines indicate the core and OS positions of the next moment, respectively. The gray cross indicates none of the association between OSs. The occurrence frequency of each condition is shown at the top of each subpanel by blue numbers. The frequency for overlaps without consideration of the OS movement is shown in parentheses by red numbers. **(e)** Examples illustrating the tracked structural evolution of OSs (i.e., development, decay, mergers and splits). The red arrows indicate the evolution of the OS with time. **(f)** Illustrations of the difference between the variable-BT_{11} and fixed-BT_{11} tracking for merger and split events. The solid red and blue lines are the CCO BT_{11} structures at different times captured by the adaptive variable-BT_{11} thresholds. The dashed red and blue contours represent the mergers and splits in the fixed-threshold tracking of 220 K.

derstood as outflowing anvil clouds from the center. It would be strange that the outflowing anvil clouds from OS2 are not connected with its origin but connected with OS1. To avoid these conditions, the distance of the nearest route is used to determine the pixel assignment. Here, the route of OS1 and OS2 to reach a pixel (the blue and red arrows in Fig. 2b) is confined to be within the 1 K interval contour. Pixels of the same distance to OS1 and OS2 are randomly assigned. In Fig. 2b, the assignment of the pixels on the basis of the distance of the nearest route is more reasonable than that in Fig. 2a on the basis of the nearest linear distance. Thus, in every 1 K interval assignment, the distance of the nearest route is used to accomplish the segmentation, and the OSs are updated with these newly assigned pixels iteratively until all the pixels within the CCO are assigned.

The final OS is the 3-dimensional (x, y and BT_{11}) structure of a single cold core. In the dimension of BT_{11}, the cold-core BT_{11} can represent its development depth, and the cold-center BT_{11} can indicate its connecting conditions with surrounding OSs in CCOs. In the horizontal dimensions of x and y, the OS area can be further separated into precipitating and non-precipitating (precipitation less than $1\,mm\,h^{-1}$) regions on the basis of the GPM. The non-precipitating area is identified as the anvil cloud. With segmentation, these precipitation and anvil pixels are explicitly associated with unique cold cores. These key definitions of variable-BT_{11} tracking are depicted in Fig. 1a and summarized in Table 1 for easy checking.

3.2 Tracking the displacement of OSs on the basis of cross-correlation

The OS displacement is derived by searching for the maximum similarity of its BT_{11} pattern in the next GEO-IR image via cross-correlation (Leese et al., 1971; Velden et al., 1998). As shown in Fig. 1b, the target scene is the OS BT_{11} pattern. The search region is centered at the core centroid of the target and confined to a radius of $50\,km$, which corresponds to a maximum cloud-drift motion of $50\,km\,h^{-1}$ (Merrill et al., 1991). The cross scene has the same shape as the OS target and refers to all possible scenes to match the OS target within the search region. The BT_{11} pattern of the target scene is normalized, as is the BT_{11} pattern of each cross scene. The pattern-matching displacement is determined by the minimum of the sum of squared differences (SSD) of the normalized BT_{11} between the OS target scene and the cross scene:

$$\mathrm{SSD} = \sum_{x,\,y} \left[\mathrm{BT}'_{11}(x,\,y) - \widetilde{\mathrm{BT}}'_{11}(x,\,y) \right]^2, \tag{6}$$

where $\mathrm{BT}'_{11}(x,\,y)$ and $\widetilde{\mathrm{BT}}'_{11}(x,\,y)$ are the normalized BT_{11} values at pixel $(x,\,y)$ of the target scene and the cross scene in the search, respectively. Here, the minimum SSD corresponds to the maximum pattern correlation. The final match is examined by the pattern correlation coefficient. For the OS

of areas larger (smaller) than $5000\,km^2$, the match is valid when the correlation of the pattern is greater than 0.6 (0.8). The correlation threshold values are consistent with those in Daniels et al. (2020). Otherwise, the OS BT_{11} structures would change rapidly in 1 h and would rather be considered stationary.

3.3 Tracking OSs via dynamic overlaps

In Fig. 1b, to track the temporal evolution of OSs, the OS is moved to the location predicted by cross-correlation and then overlaps with the OSs in the next satellite image. In this way, dynamic overlaps can be used to tolerate the fast-moving OS in tracking. For the OS with the core structure, three indices of the dynamic overlapping ratio (DOR) are considered to determine the associations of two OSs at different times, including the DOR between cores, the DOR between OSs, and the DOR between cores and OSs. The DOR between cores is the ratio of their overlaps in cores relative to the minimum area of the cores to represent the degree of core overlap. The DOR between OSs is the ratio of the OS overlap relative to the minimum area of the OS to represent the degree of OS overlap. The DOR between cores and OSs is the ratio of the overlap of the OS to the core relative to the core area, which represents the degree of the core overlapped by the OS.

Two OSs of different moments are associated in time and considered the same one OS at different times when these two OSs overlap sufficiently. With the dynamic overlap, an OS is moved to the new predicted location via cross-correlation to overlap with the OSs at the next moment. In this case, a necessary condition to consider the associations of the OSs at the next moment to the OS is that their DORs are at least greater than zero. After moving to the new predicted location, an OS might overlap with many OSs of the next moment simultaneously, and the overlapping situations are various. For instance, one OS can have large overlaps with the major core structure of an OS of the next moment, and meanwhile it can also have some overlaps with the margins of another OS of the next moment. These three DOR indices can be used to identify these distinct overlapping conditions from the overlapping degrees of their cores and OSs, as illustrated in Fig. 1c–d.

The overlapping situations of two OSs are distinguished by whether they have core overlaps (Fig. 1c) or not (Fig. 1d). A sufficient degree of overlap is discriminated by more than 50 % for DORs, which is consistent with that in Williams and Houze (1987). If their cores have overlaps, with the DOR between either cores or OSs greater than 50 %, the major parts of those pairs of OSs in situations (i), (ii) and (iv) in Fig. 1c all sufficiently overlap and thus are considered the evolution of the same OS at different times. Situation (iii) in Fig. 1c with DORs of both cores and OSs less than 50 % indicates that these two OSs only overlap in margins, with no associations in time. In Fig. 1d, when the cores of two OSs do not overlap, the determinant of the OS association relies on the
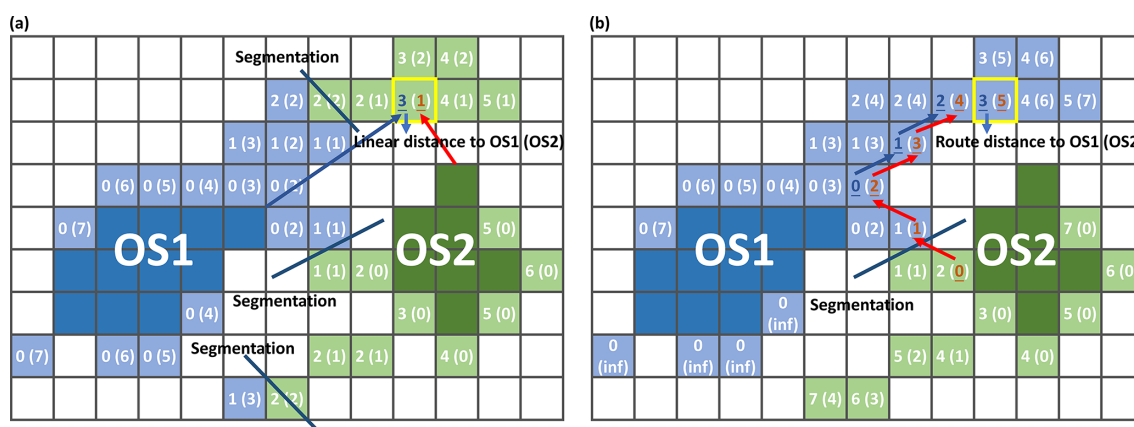
Figure 2. Illustrations of segmentation according to the nearest linear distance **(a)** and the nearest route distance **(b)**. The dark-blue and green pixels represent the OS1 and OS2 centers, respectively. The colored pixels outside the centers are the pixels to be assigned in the contour of the cold-center BT_{11} plus 1 K. The light-blue and green pixels are assigned to OS1 and OS2, respectively. The numbers inside those pixels indicate the number of necessary pixels to connect with OS1 and OS2, respectively. The arrows in panels **(a)** and **(b)** represent the nearest distances of OS1 and OS2 to reach the yellow-edge pixel, as examples to illustrate the computations of the linear distance and the route distance, respectively.

Table 1. Summary of the key definitions for variable-BT_{11} tracking developed in this study.

Name	Definition
Complex convective organizations (CCOs)	The contiguous area of the BT_{11} colder than 260 K.
Organization segments (OSs)	The segmented single-core structural component of CCOs.
Cold-core BT_{11} (OS developing depth)	The local coldest BT_{11} contour in OSs.
Cold-center BT_{11} (OS connecting depth)	The local warmest isolated BT_{11} contour of only enclosing one core.
CCO BT_{11} (CCO developing depth)	The coldest cold-core BT_{11} of multiple cores in the CCO.
Anvil clouds	The non-precipitating (precipitation less than $1\,\mathrm{mm\,h^{-1}}$) region of each OS.
Dynamic overlapping ratios (DORs)	The overlapping ratios in areas after moving it to the position predicted by cross-correlation.
Merger and split BT_{11}	The BT_{11} of the merged cold core and the BT_{11} of the splitting cold core.
Cold-core-peak BT_{11}	The coldest cold-core BT_{11} in life cycles, representing the convective peaking strength.
Development and decay stages	The stage before and after the time of the cold core peaking at the coldest BT_{11} (if there are multiple cores of the same coldest BT_{11} in the life cycle, the one of the largest core areas is selected).
Lifetime-accumulated precipitation and anvil cloud amount	The sum of the observed OS precipitation and anvil in hourly satellite images during its lifetime.

DOR between OSs and the DOR of OSs to cores. In those cases, only in situation (ii) in Fig. 1d, with large overlaps of their major parts and those two DOR indices both larger than 50 %, is the pair of OSs associated in time. Those pairs of OSs in the other situations in Fig. 1d are obviously not associated. Overall, if the DORs of two OSs satisfy the overlapping conditions of (i), (ii) and (iv) in Fig. 1c and (ii) in Fig. 1d, they are associated in time and regarded as the same OS evolving with time.

In Fig. 1c–d, the occurrence frequency of those overlapping conditions is listed at the top of each subpanel (the blue numbers), in which the red numbers in the parentheses refer to the frequency for conventional stationary overlaps without consideration of the OS movement. Here, every pair of OSs with overlaps is counted as one sample. For instance, if one OS has overlaps with five OSs of the next moment, there are five pairs of overlapping OSs, and the sample number is five. The frequency is defined as the occurrence of each overlapping condition in Fig. 1c–d divided by the total sample number. It is not surprising that the condition of (iii) in Fig. 1d accounts for the largest portion of samples, since the OSs in CCOs are close to each other, and their margins easily

overlap. Compared with the stationary overlaps, the dynamic overlaps increase the frequency of the overlapping condition of (ii) of Fig. 1c 2-fold and decrease the frequency of all other conditions. Overall, the dynamic overlaps increase the frequency of associations (the sum of frequencies of (i), (ii) and (iv) in Fig. 1c and (ii) in Fig. 1d) by 2.5 % from 21.2 % (the frequency of associations for stationary overlaps) to 23.7 %.

For two temporally associated OSs, the development and decay can be inferred from the variation in the cold-core BT_{11} and area, as shown in Fig. 1e. The variation in the cold-core BT_{11} is considered first before the variation in the cold-core areas for discriminating between development and decay. If the cold-core BT_{11} is colder with time, or if the cold-core BT_{11} is the same but the cold-core area is larger with time, the OS is developing; otherwise, it decays. Notably, OSs are not necessarily associated with only one OS. As shown in Fig. 1e, mergers and splits are allowed in dynamic overlaps and are identified as the many-to-one and one-to-many OS associations, respectively. The merged cold-core BT_{11} and the splitting cold-core BT_{11} are documented as the BT_{11} of mergers and splits, respectively.

In comparison, conventional fixed-threshold tracking infers development and decay from the variation in the area, in which the tracking target might be very complicated and involve multiple convective activities at different life stages. However, the variable-BT_{11} tracking infers the development and decay of each partitioned OS from the variation in both the cold-core BT_{11} and the area. Additionally, mergers and splits in fixed-threshold tracking are dependent on the selection of the BT_{11} threshold. Owing to the selection of the fixed BT_{11} threshold, convective systems are usually connected under a warmer threshold but are disconnected under a colder threshold. As illustrated in Fig. 1f, under the fixed threshold of 260 K, no mergers or splits occur. Under the fixed threshold of 220 K, the cutoff of the CCO by 220 K is the connected complex of multiple cores or two disconnected parts at different times. This change in the connecting conditions over time under the selected fixed threshold results in mergers and splits in fixed-threshold tracking. Under the fixed threshold of 200 K, the mergers and splits of cold cores are captured. It manifests that mergers and splits in fixed-threshold tracking can be attributed to many reasons: threshold selection, changes in the connecting conditions and variations in cold cores over time. In contrast, in variable-BT_{11} tracking, mergers and splits are not influenced by changes in the connecting conditions over time but are related only to the variation in cold cores, as illustrated in Fig. 1e–f.

3.4 Quality control and validation of variable-BT_{11} segment tracking

Quality control for missing images and the OSs touching the image edges is conducted. If the missing time gap between two satellite images exceeds 2 h, the OSs in these two images and all life cycles of these OSs are excluded from the analy-

ses. Additionally, the OSs touching the image edges and all life cycles of the OSs touching the edges are excluded.

There are no direct observations to validate whether OSs are correctly associated. However, some of the tracked behaviors (e.g., the tracked motions of OSs) can be examined against the measurements of other sensors. Only if the tracking is correct would the derived OS-drift winds perform well. Thus, the OS-drift winds are compared against the radiosonde cloud-top winds at three ARM tropical sites in Darwin, Manus and Nauru. Here, the cloud-top winds are derived by combining the radar and radiosonde observations at those sites (see more details in Sect. 2.3) as the observational reference to examine the tracked OS motions from the hourly satellite images in 2006. To collocate the observations from the ground-based sites and satellites, the tracked OS-drift winds from the GEO observations that are closest to the time of the cloud-top wind observations and nearest to the site locations are used to compare with the cloud-top winds at those ground-based sites. The observational time difference is no more than 1 h, and the tracked OS core centroid is within 150 km of those ARM site locations. These settings are consistent with those of previous studies in which the performance of cloud-drift winds was examined (Nieman et al., 1997; Santek et al., 2019; Daniels et al., 2020).

In Fig. 3, the OS-drift winds are significantly correlated with the radiosonde cloud-top winds. The correlations are 0.52 and 0.45 at the 99 % significance level for the U and V wind components, respectively. On average, the OS-drift winds are slower than the radiosonde-observed winds are, with a mean bias of $-1.6\,\mathrm{m\,s^{-1}}$. A slow speed bias of $1\text{–}2\,\mathrm{m\,s^{-1}}$ is common for cloud-drift winds (Santek et al., 2019). Owing to the limitations of the spatial and temporal resolutions (5 km and 1 h, respectively), the least identifiable speed variation is approximately $5\,\mathrm{km\,h^{-1}}$ ($1.4\,\mathrm{m\,s^{-1}}$), which is a possible reason for the slow speed bias. The bias in the mean angle is very small (0.5°). The MVD, SD and RMSE are 6.9, 4.7 and $8.4\,\mathrm{m\,s^{-1}}$, respectively. These biases are not surprising since real-world clouds do not strictly flow with ambient winds. In addition, some bias might be attributed to the uncertainty in the cloud-top heights. For its detection, the MMCR might underestimate the cloud-top height since its signal would attenuate quickly for deep convective clouds (Hollars et al., 2004). In convective systems, the motion of air is highly organized (Houze, 2004); thus, system movement might be inconsistent with the observed winds at the cloud-top height. Typically, the RMSE of the vector between the cloud-drift winds and the reference cloud-top winds is approximately $6\text{–}13\,\mathrm{m\,s^{-1}}$, according to previous studies (Santek et al., 2019; Bresky et al., 2012). This finding indicates that the tracked motions of OSs are reasonable, and thereby variable-BT_{11} segment tracking is appropriate.
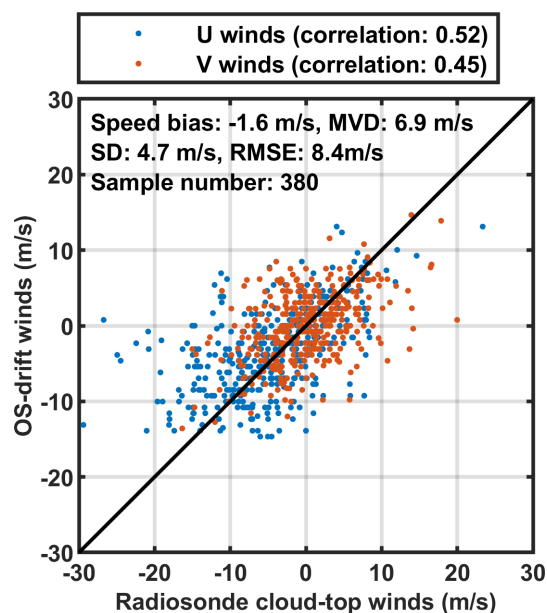
Figure 3. Comparisons of the U and V wind speeds between the tracked motions and radiosonde cloud-top winds within 150 km at Darwin, Manus and Nauru in 2006, with a total sample number of 380.

3.5 Comparison with conventional fixed-threshold tracking

The fundamental difference between fixed-threshold and variable-BT_{11} tracking is target selection. With the fixed threshold of BT_{11}, the connected convections of multiple cold cores are identified as tracking targets, and only the area information is accessible for their life cycles. With the OS as tracking targets, variable-BT_{11} tracking is capable of documenting the detailed evolution of each OS within CCOs, such as the developing depth, connecting conditions, and contributions to precipitation and anvil clouds.

The complexity of convective organizations determines the use of fixed-threshold or variable-BT_{11} tracking. Specifically, if the structure of convection is simple with only one cold core, it can be simply tracked via fixed-threshold tracking. Otherwise, for the complex organization of connected convective activities with multiple cold cores, variable-BT_{11} tracking is suitable since it is capable of segmenting CCOs into OSs for tracking.

In Fig. 4, the OS structural characteristics (i.e., the connecting conditions with other surrounding OSs in CCOs and their contributions to precipitation and anvil cloud areas) of different development depths with the cold-core BT_{11} from 190–250 K are investigated. In Fig. 4a, for the OSs of the cold core from 190–250 K, the probability distribution functions (PDFs) of the cold-center BT_{11} are shown. The cold-core and cold-center BT_{11} are both identified by 5 K interval adaptive thresholds (see details in Sect. 3.1). The PDFs in Fig. 4a have a maximum peak of approximately 36 %–41 %

when the cold-center BT_{11} is equal to the cold-core BT_{11}. This implies that for most of them, only the cold core can be isolated by the fixed threshold. For the deep convection of the cold-core BT_{11} at 190–220 K, the isolated structure with a cold-center BT_{11} of 260 K is rare, but it is relatively more frequent and seems to be another mode for the shallow warm systems of the cold-core BT_{11} at 230–250 K. However, fixed-threshold tracking is not capable of discriminating between isolated and complicated structures.

There is no doubt that the warmer the selected BT_{11} threshold is, the more complex the identified target is in the fixed-threshold identification. However, can a cold BT_{11} threshold be used to avoid complicated connected convective organizations? If feasible, the fixed-BT_{11} tracking under the cold threshold performs well. For instance, Feng et al. (2018) tried to use two thresholds to identify convective systems with a cold threshold of 225 K to capture the cold core and a warm threshold of 241 K to find the cloud pixels associated with the cold cores. In this case, is the 225 K cutoff a simple or complicated structure? If under the fixed threshold of 225 K, Fig. 4a shows the following:

1. For the OSs of the cold-core BT_{11} from 230–250 K, they would be ignored since these OSs develop warmer than 225 K.

2. For the OSs of the cold-core BT_{11} from 190–220 K and the cold-center BT_{11} from 190–220 K, they would be in complicated convective organizations and cannot be simply identified by the fixed threshold of 225 K.

3. For the OSs of the cold-core BT_{11} from 190–220 K and the cold-center BT_{11} from 225–260 K, they can be directly isolated by the fixed threshold of 225 K, but it accounts for only a small portion of the OSs of the cold-core BT_{11} from 190–220 K.

This implies that even under the cold BT_{11} threshold, most of the identified targets still have complex organizations.

Figure 4b shows the PDFs of CCO BT_{11}, which refers to the coldest cold-core BT_{11} in the CCO. The CCO BT_{11} can help to further distinguish the connecting conditions of the OS at different depths of development. If the CCO BT_{11} is colder than the OS cold-core BT_{11}, the OS is in a deeper CCO and connected with a colder OS. Otherwise, if the CCO BT_{11} is equal to the OS cold-core BT_{11}, the OS is the isolated structure or connected with a warmer OS. For the OSs of the cold-core BT_{11} from 200–260 K, the PDFs of the CCO BT_{11} all peak at 195 K. This implies that they are the most frequently clustered in the 195 K CCO. For the OSs of cold-core BT_{11} from 230–260 K, another peak of the PDFs of their CCO BT_{11} is at their cold-core BT_{11}. Figure 4a also shows that these OSs of the cold-core BT_{11} from 230–260 K are more likely to have the cold-center BT_{11} occurring at 260 K. This implies that warm-core structures are more likely to be isolated than cold-core structures. As a result, deep convective activities are mostly accompanied by the clustered
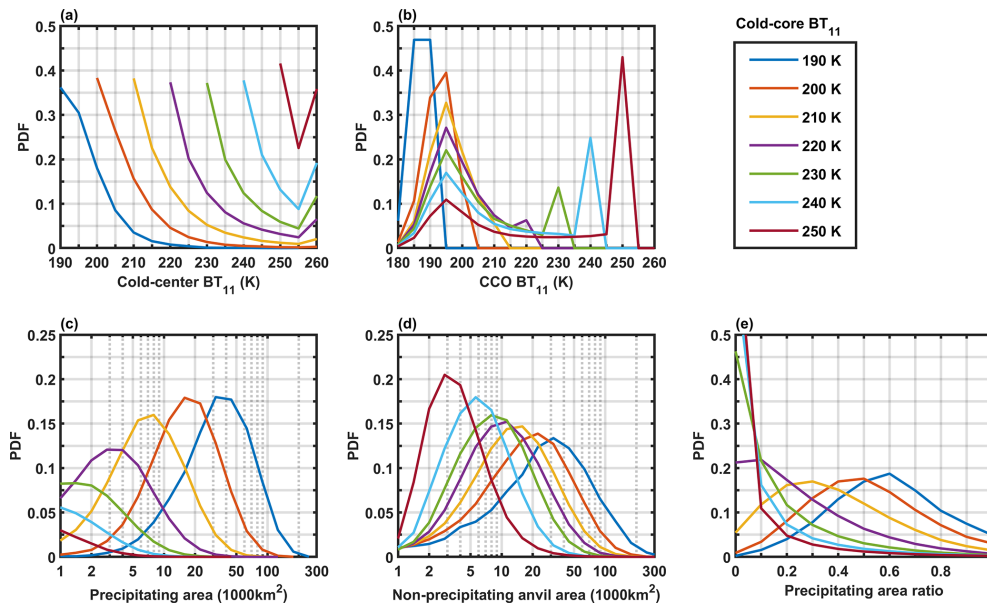
Figure 4. The OS structural characteristics of CCOs. PDFs of cold-center BT_{11} (**a**), CCO BT_{11} (**b**), the precipitating area (**c**), the non-precipitating area (**d**), and the ratio of the precipitating area (**e**) for the OSs of the cold-core BT_{11} from 190–250 K.

complex organization, and variable-BT_{11} segment tracking is more suitable than fixed-threshold tracking for documenting their behaviors.

In variable-BT_{11} tracking, precipitation and anvil clouds can be explicitly attributed to unique cold cores. In Fig. 4c–d, the distributions of the precipitation and anvil areas are lognormal and closely related to cold-core BT_{11}. The colder the cold-core BT_{11} is, the greater the precipitation and anvil areas the OS contributes to. In Fig. 4e, the ratio of the OS precipitation area to the whole OS area is inversely proportional to the cold-core BT_{11}. The OSs of colder cores are dominated by more precipitation, and these OSs still contribute to more anvil clouds than the OSs of warmer cores. Similar to Lindzen et al. (2001), the ratio of the OS precipitation area to the whole OS area can also be understood as a diagnostic of the precipitation efficiency or detrainment effect. In Fig. 4c–e, the observed relationship between the BT_{11} structure and precipitation efficiency might be expected. Storms with higher precipitation efficiency generally have less dry air entrainment, which may allow updrafts to reach higher altitudes and lower BT_{11}.

Examples of the conventional fixed-threshold and novel variable-BT_{11} tracking algorithms are shown in Fig. 5 to illustrate their differences. From the GEO images in the uppermost panel of Fig. 5, visually, those convective activities are connected in CCOs but have distinct behaviors to decay, split, develop and merge over time. In the middle panel of Fig. 5, these behaviors of connected convections are barely distinguished by fixed-threshold tracking. With thresholds of 235 and 260 K, the whole complex organization of connected convections is identified as the tracking target. By

the cold threshold of 210 K, only a small part of the CCO is identified; nevertheless, those connected convections of distinct behaviors are still poorly distinguished. Additionally, in fixed-threshold tracking at 210 K, mergers and splits are caused by variations in whether convections are connected under the 210 K threshold. In this case, the tree of the tracked life cycle is too complicated to analyze and is usually simplified by focusing only on the largest area at different times as the major branch of the life cycle. The major branch (the red line in the middle panel of Fig. 5) begins with the large complex organization of connected convections but ends with only one of disconnected parts. Only the area information is available to describe the life cycle in fixed-threshold tracking. In comparison, in the bottom panel of Fig. 5, on the basis of adaptive variable-BT_{11} identification and segment tracking, these connected convective activities are separately tracked as the decaying and splitting no. 3 OS, developing no. 2 OS, merging and developing no. 4 OS, etc. The mergers and splits of OSs are well tracked and not influenced by the variations in the connecting conditions over time. The area information and cold-core BT_{11} information are both available to describe the tracked life cycles.

4   Relationships of precipitation and anvil production with the structural evolution of BT_{11} for oceanic convection over the tropical western Pacific Ocean

The warm pool of the tropical western Pacific Ocean (20° S–20° N, 130° W–170° E) is a typical region of oceanic convection that precipitates and produces anvil clouds (Wall et
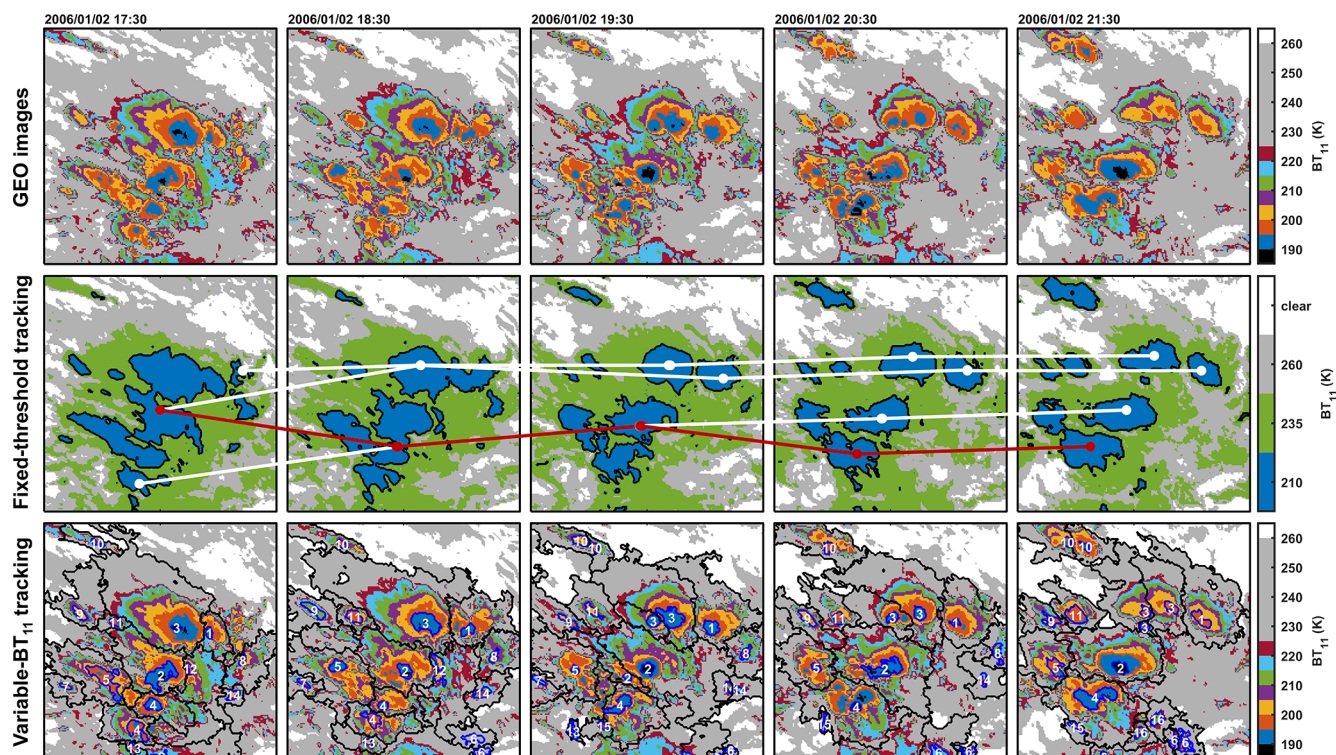
Figure 5. Examples illustrating the difference between conventional fixed-threshold tracking and novel variable-BT_{11} segment tracking. Uppermost panels: GEO BT_{11} images taken between 5–15° S and 120–130° E from 2 January, 17:30 to 21:30 UTC in 2006. Middle panels: the tracked life cycles based on the fixed thresholds of 210, 235 and 260 K. The white lines represent the tree of the tracked life cycle under the fixed threshold of 210 K, and the red lines represent the major branch obtained by selecting the largest area. Bottom panels: variable-BT_{11} identification and segment tracking. In the bottom panels, the blue contours indicate the cold cores, the black contours are the OSs in the CCOs and the number at the core centroids indicates the identification number of life cycles.

al., 2018). In this section, only the CCOs and OSs over the oceans in this region are considered for investigating the behaviors of the oceanic convection precipitating and producing anvil clouds. Notably, the anvil identification requires that the BT_{11} is colder than 260 K and the precipitation is less than 1 mm h^{-1}. It can be used to reflect the anvil productivity in the convective systems (Yuan and Houze, 2010; Yuan et al., 2011; Yuan and Houze, 2013), but much of the area of detrained cirrus has a BT_{11} warmer than 260 K in reality (Gasparini et al., 2022; Sokol and Hartmann, 2020; Berry and Mace, 2014). Normally, these thin cirrus clouds are not well identified by GEO radiometers, and thus in this work, the anvil just refers to the thick anvil portion identified by the 260 K BT_{11} threshold but not all detrained anvil cirrus clouds.

The total precipitation and anvil cloud amounts of convection are important for tropical water and radiative budgets. They can be attributed to two factors: (1) the occurrence frequency of convection and (2) the precipitation and anvil production for the duration of convection. However, over the warm pool of tropical oceans, convective activities are clustered in CCOs, and their precipitation and produced anvil clouds are merged (as discussed in Sect. 3). As a result, iden-

tifying their contributions to precipitation and anvil clouds is difficult. On the other hand, the CCO is a large cluster for a series of alternating successive convective activities, which are initiated at different times and evolve in different ways. Thus, there is a dilemma in tracking convection: convection is not isolated naturally for tracking, whereas the CCO is the envelope of many convections whose precipitating and anvil areas are mixed, and it is difficult to identify single convective processes from the CCO life cycle.

It has long been well observed by various active and passive sensors that tropical convections have core structures, e.g., convective pillars observed by active sensors (Igel et al., 2014; Takahashi and Luo, 2012; Deng et al., 2016), heavy raining cores observed by radar or passive microwave radiometer (Yuan and Houze, 2010; Feng et al., 2011), and cold cores of BT_{11} observed by GEO or MODIS radiometers (Yuan and Houze, 2010; La and Messager, 2021; Yang et al., 2023). Although convective structures can be better identified by active sensors than by passive sensors, active sensors are only available at a limited number of ground-based sites or on polar-orbit satellites, and their samplings are too sparse for tracking. Yuan and Houze (2010) and Yang et al. (2023) both used active and passive sensors in combina-

tion and demonstrated that the BT_{11} structures are strongly associated with the convective structures. Yuan and Houze (2010) reported that cold BT_{11} and warm BT_{11} correspond to two distinct types of clouds detected by active sensors: very deep convective clouds and elevated anvil clouds. They partitioned the CCO into single-core high cloud systems (i.e., the OS defined in this work) and identified those OSs with heavy precipitation and a cold-core BT_{11} colder than 220 K as mesoscale convective systems (MCSs). For these MCSs, Yuan et al. (2011) observed that the cloud vertical structures are well organized, in which high-topped clouds extend outward from raining cores, and the thickness of the anvil and the sizes of ice particles are closely related to the distance to the raining cores. Similarly, Yang et al. (2023) identified the cold cores of BT_{11} as convective centers and also found that the cold-core structures of BT_{11} are highly consistent with the convective structures detected by active sensors. These findings suggest that cold cores of BT_{11} can be used to identify the most convective-developing centers and distinguish convective activities in CCOs. In Sect. 3, a novel algorithm was developed to accomplish tracking for convective cold-core structures on the basis of previous studies (Yuan and Houze, 2010; Yuan et al., 2011) and GEO observations.

These OSs can be used to infer different convective activities clustered in CCOs. They are organized differently with various depths of development, precipitation and anvil production and have distinct evolution processes. In this section, on the basis of variable-BT_{11} tracking, the relationships of convective contributions to precipitation and anvil clouds with their BT_{11} structural evolution are explored. This would provide an opportunity to compare convections of different development strengths and evolution processes for their contributions to precipitation and anvil clouds.

4.1 Relationships of lifetime-accumulated precipitation and anvil clouds with cold-core-peak BT_{11}

Figure 6 illustrates an idealized tracking for a CCO and its OSs. The real-world CCO tracking can be much longer and more complicated than that in Fig. 6, and here, it is just used to illustrate how to understand the CCO and OS tracking. As illustrated in Fig. 6, the CCO tracking (dashed black line) can capture the variation in precipitation and anvil areas contributed by multiple convections, but it does not link these variations to specific convections. Mergers and splits in the CCO life cycle reflect the connections and disconnections between different convections. With the OS tracking, the CCO life cycle can be decomposed into the life cycles of its structural components (the colored lines in Fig. 6). It can be recognized that the life cycle of the CCO starts with three convective activities, and with time two of them are merged into the OS1 life cycle, and the right one splits into two as the OS2 life cycle. In this way, precipitation and anvil clouds are associated with convective activities in CCOs. On the other hand, the CCO is a large envelope of many convective ac-
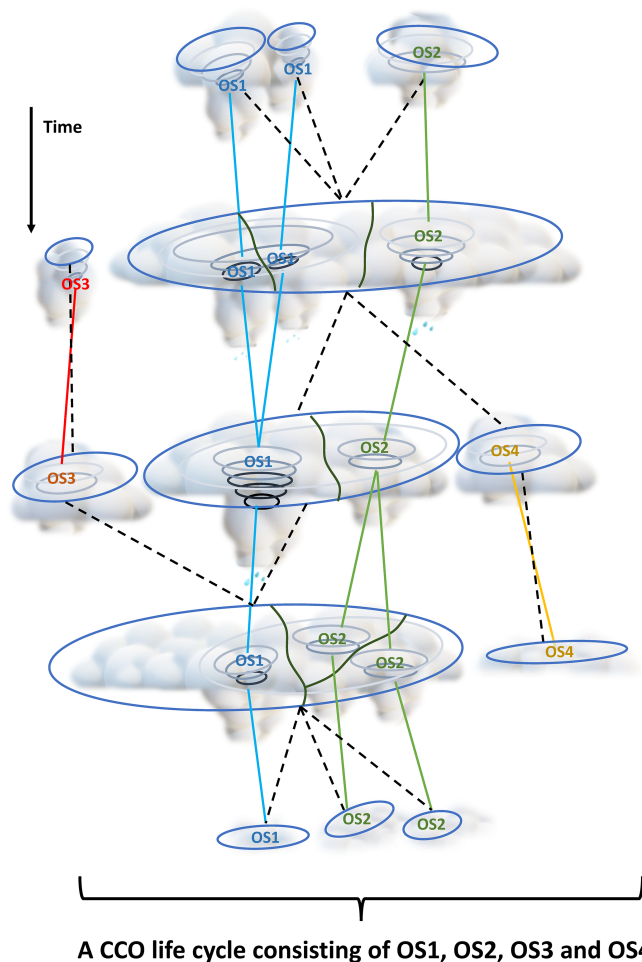
A CCO life cycle consisting of OS1, OS2, OS3 and OS4

Figure 6. Illustrations of the difference between tracking a CCO and tracking OSs. The CCO life cycle include four OS life cycles. The dashed black line indicates the tree of the CCO life cycle. The blue, green, red and yellow lines indicate the tree of OS1, OS2, OS3 and OS4 life cycles, respectively.

tivities, and it is not expected that they all have simple perfect life cycles from convective initiation to anvil dissipation. The OS might just be borne from the split of the anvil or the secondary convective activity in its parent stronger convective body (e.g., the OS4 life cycle in Fig. 6) and ends by merging into the anvil in the CCO (e.g., the OS3 life cycle in Fig. 6). The OS tracking documents the life cycle of the core structure from initiation to dissipation. It can be expected that the active convective activities have robust and durable core structures in CCOs, while weak secondary convective activities are fragile and short-lived. In Figs. 7 and 8, the basic features of OS life cycles of different peaking strengths are investigated for their occurrence, duration, and contributions to precipitation and anvil clouds.

For OS life cycles, the cold-core-peak BT_{11} is identified as the coldest cold-core BT_{11} in life cycles and is used to represent the convective peaking strength. The OS life cycles
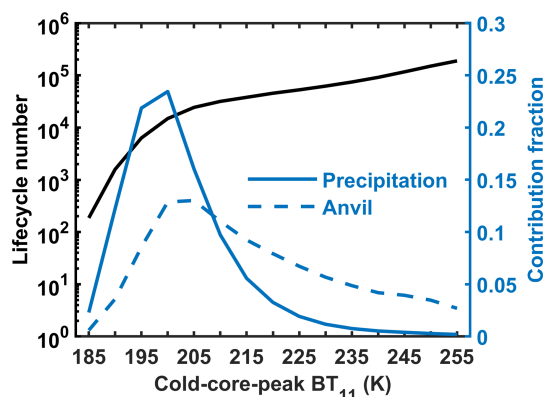
Figure 7. Sample numbers of tracked OS life cycles with cold-core-peak BT_{11} values from 185–255 K in the tropical western Pacific (20° S–20° N, 130° W–170° E) in 2006. The contribution fractions of the OS life cycles to the precipitation and anvil cloud amounts are shown on the right y axis.

are classified by the cold-core-peak BT_{11}. In Fig. 7, the sample numbers of life cycles of different cold-core-peak BT_{11} values over the tropical western Pacific Ocean in 2006 are shown. The warmer the cold-core-peak BT_{11} is, the greater the number of life cycles is. The life cycle of the cold-core-peak BT_{11} at 185 K only has over 100 samples, and the life cycle of the cold-core-peak BT_{11} at 255 K has hundreds of thousands of samples in 1 year. In addition, Fig. 7 also shows the fractions of the contributions of OS life cycles of different cold-core-peak BT_{11} values to the total precipitation and anvil cloud amounts. Here, the fraction of contribution refers to the sum of the precipitation (anvil) produced by all OS life cycles in each bin of the cold-core-peak BT_{11} divided by the total precipitation (anvil). The OS life cycles of the cold-core-peak BT_{11} at 200 K have the largest contribution to both the precipitation and anvil cloud amounts. Although the life cycles of the cold-core-peak BT_{11} values warmer than 235 K have a great number of samples, those life cycles only contribute to no more than 5 % of the total precipitation and anvil cloud amounts. Nevertheless, those warm structures seem to be more important for anvil clouds than for precipitation.

In Fig. 8a–c, for different cold-core-peak BT_{11} values, the PDFs of the OS duration, and the OS lifetime-accumulated precipitation and anvil amount are shown. Here, the OS duration refers to the length in time of the tracked OS life cycle. The OS lifetime-accumulated precipitation and anvil amount are the sum of the observed OS precipitation and anvil in hourly satellite images during its lifetime. For example, for the OS1 life cycle in Fig. 6, the lifetime-accumulated precipitation and anvil amount are the sum of the hourly precipitation and anvil in the OS1 life tree.

In Fig. 8a, for the duration of the OS with the cold-core-peak BT_{11} warmer than 220 K, the PDFs peak at 1 h, and most of the durations are less than 5 h. For the life cycle of the peak BT_{11} colder than 220 K, the OS duration has two

modes: short-lived (1–4 h) and long-lived (at least 5 h). As discussed previously, it is not expected that convective activities in CCOs all have simple perfect life cycles from convective initiation to anvil dissipation. Some OSs, even for those very cold structures, are just very short-lived overshooting, with only a 1 h duration for the secondary convective activity in its parent stronger convective body, and then disappear or may be annexed by their surrounding stronger vertical-developing convection in CCOs.

In Fig. 8b–c, the PDFs of the accumulated precipitation and anvil amounts contributed by the OS life cycles basically conform to the lognormal distribution. Overall, the duration, precipitation and anvil amount of lifetime accumulation are inversely proportional to the cold-core-peak BT_{11}.

In Fig. 8d–f, the relationships of the OS duration and the OS lifetime-accumulated precipitation and anvil amount with the cold-core-peak BT_{11} are further investigated. The OS life cycle is separated into development and decay stages. The development (decay) stage is defined as the stage before (after) the cold core peaks at the coldest BT_{11} with the largest core area. The peak is counted as the decay stage. Thus, for short-lived OSs with a duration of only 1 h, their decay time is just 1 h, and the development time is zero. In Fig. 8d, only the OS life cycles of the cold-core-peak BT_{11} colder than 220 K have a development of more than 1 h, whereas the OS life cycles of the peak BT_{11} that is warmer than 220 K directly decay and disappear rapidly within a few hours. This implies that most of these warm structures are just the anvil split with weak secondary convection from its main convective body (such as the OS4 in Fig. 6). On the basis of the PDFs of the OS duration (Fig. 8a) and the duration of development and decay (Fig. 8d), those OSs with a cold-core-peak BT_{11} colder than 220 K and durations greater than 5 h are identified as active convective activities; otherwise, the OSs with warmer or short-lived core structures are weak secondary convective activities.

Figure 8d–f show that the process of decay is longer than the process of development and that more precipitation and anvil clouds are contributed by the process of decay than by the process of development. Overall, the OS duration and the lifetime-accumulated precipitation and anvil amount have simple loglinear relationships with the peak BT_{11} in both the development and decay stages. The difference in the duration and the accumulated precipitation and anvil cloud amounts between the two stages (the black line in Fig. 8d–f) also exponentially increases, with the core peaking at colder BT_{11} values. The duration of the development and decay processes and the two key components of the convective cloud water budget, i.e., the lifetime-accumulated precipitation and anvil cloud amounts, are closely related to the peaking cold-core structures.

4.2 Influence of mergers and splits on precipitation and anvil production

Mergers and splits represent activities of cold cores in the OS tracking. In Fig. 9a, according to the PDFs of the cold-core BT_{11} of mergers and splits, the cold-core BT_{11} of mergers is distributed at colder BT_{11} values than that of splits. This implies that mergers are more likely to occur for cold structures, whereas splits are more likely to occur for warm structures. Figure 9b–c show the occurrence frequency of mergers and splits in the OS life cycles of different cold-core-peak BT_{11} values, in the development and decay stages, respectively. It is somewhat surprising that the frequency of mergers and splits still has a loglinear relationship with the cold-core-peak BT_{11}. In the development process, mergers are more likely to occur than splits. In the decay process, mergers and splits have similar occurrence frequencies, but the splits in the decay process are more frequent than those in the development process.

According to the occurrence of mergers and splits, OS life cycles can be further classified into simple (no mergers or splits), only-merger, only-split and complicated (both mergers and splits) types. In Fig. 10a–c, the lifetime-accumulated precipitation, anvil cloud amount and duration are strongly related to the occurrence of mergers and splits. For the same cold-core-peak BT_{11}, the complicated life cycles have the largest accumulated precipitation, anvil and duration among all types of life cycles. The only-merger and only-split life cycles have similar accumulated precipitation, anvil and duration values that are greater than those of the simple life cycles. Interestingly, for different types of life cycles, the slopes of the loglinear relationships of the lifetime-accumulated precipitation, anvil and duration with the cold-core-peak BT_{11} are nearly invariant. This implies that mergers and splits do not influence the dependence of the lifetime-accumulated precipitation and anvil cloud amounts on the BT_{11} structures and that the increased precipitation and anvil cloud amounts caused by the mergers and splits also conform to a loglinear relationship with the cold-core-peak BT_{11}.

How do mergers and splits influence the lifetime-accumulated precipitation and anvil cloud amounts? This question is simply explored from the OS tracking. In the OS life cycle, the variation in the accumulated precipitation and anvil cloud amounts can be attributed to two possible factors: (1) the hourly precipitation and anvil production in the life cycle are enhanced by mergers and splits, and (2) the lifetime is prolonged by mergers and splits.

In Fig. 11a–b, the hourly mean precipitation and anvil amount in the OS life cycles are shown for different types of life cycles. For the same cold-core-peak BT_{11}, the hourly mean precipitation of different life cycle types is nearly invariant (Fig. 11a). However, in the life cycles with the occurrence of mergers and splits, the hourly mean anvil production is enhanced (Fig. 11b), and the lifetime (L) is significantly prolonged (Fig. 10c). To quantify their impacts, in Fig. 11c–d, the anomalies of the lifetime-accumulated precipitation and anvil cloud amounts can be decomposed as follows:

$$PL - \overline{P}\,\overline{L} = \overline{L}P' + \overline{P}L' + P'L', \qquad (7)$$

$$AL - \overline{A}\,\overline{L} = \overline{L}A' + \overline{A}L' + A'L'. \qquad (8)$$

P and A are the hourly precipitation and anvil cloud amount, respectively. L is the lifetime. Thus, PL and AL represent the lifetime-accumulated precipitation and anvil cloud amount, respectively. The bar over the letter represents the mean of different life cycle types. The prime over the letter represents the anomaly of different life cycle types relative to their mean value. In this way, $\overline{L}P'$ and $\overline{P}L'$ indicate the contributions of the hourly precipitation anomaly and the lifetime anomaly, respectively, to the variation in lifetime-accumulated precipitation. Similarly, $\overline{L}A'$ and $\overline{A}L'$ indicate the contributions of the hourly anvil production and lifetime anomalies, respectively, to the variation in the lifetime-accumulated anvil amount. $P'L'$ and $A'L'$ are high-order small quantities and are neglected. The fraction of the contribution can be computed by dividing the left-hand-side quantities of Eqs. (7) and (8). Figure 11c (Fig. 11d) shows the fractions of the contributions of $\overline{L}P'$ and $\overline{P}L'$ ($\overline{L}A'$ and $\overline{A}L'$) to the increase in lifetime-accumulated precipitation (anvil) from simple to complicated life cycles. For the life cycles of the cold-core-peak BT_{11} colder than 220 K, $\overline{L}P'$ has a relatively small contribution of approximately 10 %–25 %, whereas $\overline{P}L'$ has a large contribution of approximately 60 %–80 %. In addition, $\overline{L}A'$ and $\overline{A}L'$ both have positive comparable contribution fractions, approximately 20 %–40 % and 40 %–60 %, respectively. For the warmer life cycles, the contributions from $\overline{L}P'$ and $\overline{L}A'$ increase and are more important than the lifetime anomaly for the variation in the lifetime-accumulated precipitation and anvil cloud amounts.

On average, in comparison with simple life cycles, mergers and splits can significantly prolong the duration of OSs while enhancing the hourly precipitation slightly and increasing the hourly anvil production strongly. From simple to complicated life cycles, a prolonged lifetime accounts for the largest contribution to the increase in accumulated precipitation and anvil clouds for cold structures.

4.3 Contributions of the OS life cycles to the total precipitation and anvil cloud amount

Figures 8–11 show that the OS duration and the lifetime-accumulated precipitation and anvil cloud amounts all have loglinear relationships with the cold-core-peak BT_{11} and are positively related to the occurrence of mergers and splits. However, the life cycles of cold structures are less common than the life cycles of warm structures and thus might make only small contributions to the total precipitation and anvil clouds (Fig. 7). In Fig. 12, the contributions of the OS life
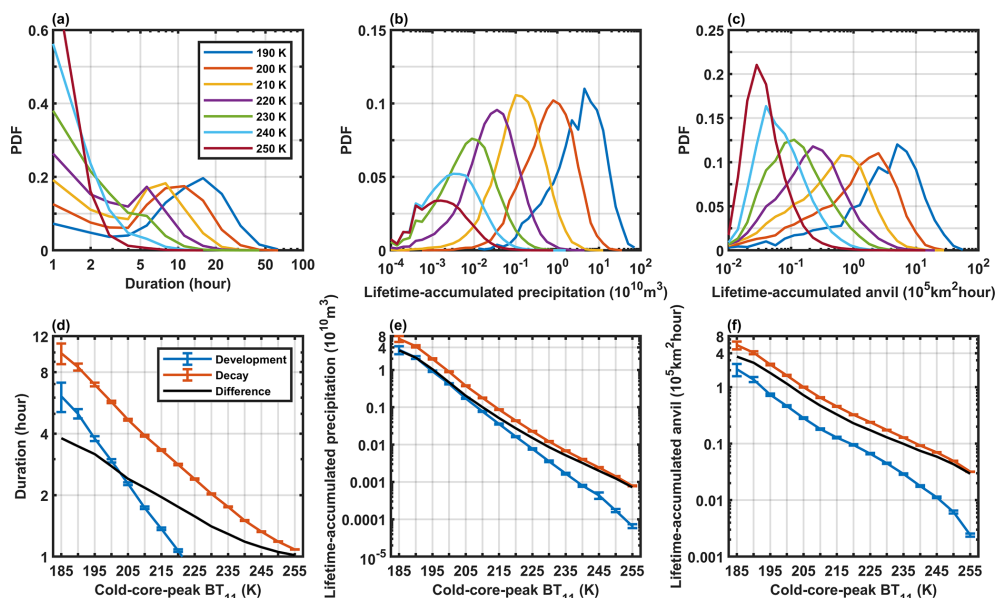
Figure 8. PDFs of the duration (**a**), precipitation (**b**) and non-precipitating anvil amount (**c**) of lifetime accumulation, for the OS life cycles of different cold-core-peak BT_{11} values from 190–250 K. The composites of the duration (**d**) and the lifetime-accumulated precipitation (**e**) and anvil amount (**f**) contributed by the development (blue lines) and decay stages (red lines) as a function of the cold-core-peak BT_{11} from 185–255 K. The black lines represent the differences in the duration and the lifetime-accumulated precipitation and anvil between the development and decay stages in panels (**d**)–(**f**), respectively. The error bars indicate the 95 % confidence intervals of the means based on the t test.
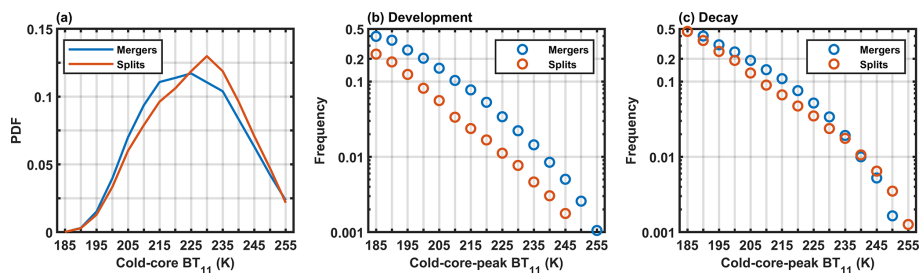
Figure 9. (**a**) PDFs of BT_{11} values for mergers (blue lines) and splits (red lines). The occurrence frequency of mergers and splits in the life cycles of the cold-core-peak BT_{11} from 185–255 K in the development (**b**) and decay (**c**) stages.
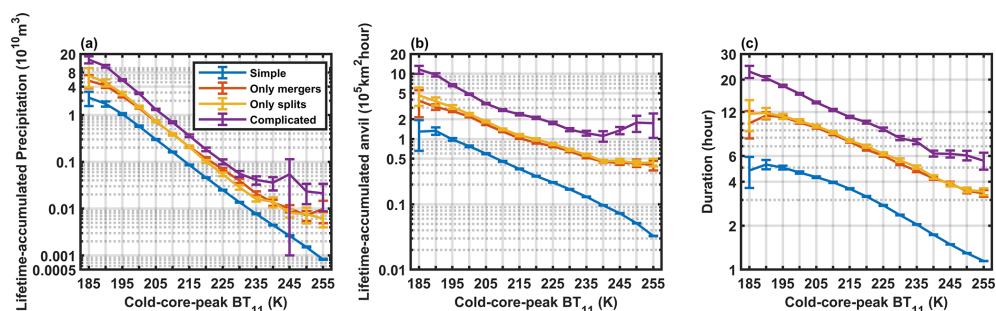
Figure 10. Composites of the lifetime-accumulated precipitation (**a**), anvil cloud amounts (**b**) and durations (**c**) of different life cycle types in each bin of the cold-core-peak BT_{11} from 185–255 K. The blue, red, yellow and purple lines indicate the simple, only-merger, only-split and complicated life cycles, respectively. The error bars indicate the 95 % confidence intervals of the means based on the t test.
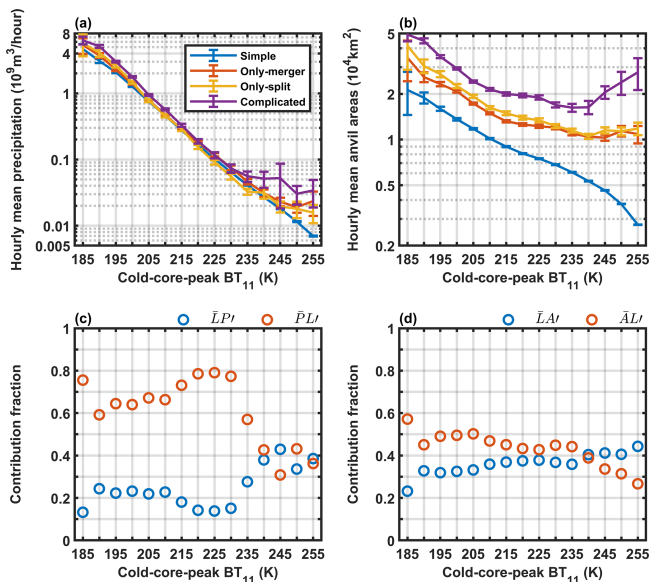
Figure 11. Composites of the hourly mean precipitation **(a)** and anvil cloud amounts **(b)** of different life cycle types in each bin of the cold-core-peak BT_{11}. The blue, red, yellow and purple lines indicate the simple, only-merger, only-split and complicated life cycles, respectively. **(c)** The fractions of contributions of the hourly precipitation anomalies ($\bar{L}P'$) and lifetime anomalies ($\bar{P}L'$) to the variation in lifetime-accumulated precipitation. **(d)** The fractions of contributions of the hourly anvil production anomalies ($\bar{L}A'$) and lifetime anomalies ($\bar{A}L'$) to the variation in the lifetime-accumulated anvil amount. The error bars indicate the 95 % confidence intervals of the means based on the t test.

cycles of different cold-core-peak BT_{11} values and durations to the total precipitation and anvil cloud amounts are shown.

The simple life cycle without mergers and splits is the most frequent and accounts for 93.9 % of samples. The only-merger, only-split and complicated life cycle have the frequency of only 3.0 %, 1.4 % and 1.7 %, respectively. However, these life cycles with mergers and splits can contribute to a large portion of total precipitation and anvil clouds. For precipitation, as shown in Fig. 12a–d, the complicated life cycles have the largest contribution of 45.6 %, compared with the simple (29.1 %), only-merger (18 %) and only-split (7.3 %) life cycles. The cold long-lived life cycles (active convective activities) with the cold-core-peak BT_{11} colder than 220 K and durations of at least 5 h contribute to 84.8 % of the total precipitation, in which the life cycles with mergers and splits contribute to the largest portion (68.7 %). This implies that the cold long-lived life cycles with merger and split activities are the most important for precipitation.

For the non-precipitating anvil clouds in Fig. 12e–h, the cold long-lived life cycles still have the largest contribution fraction (60.5 %), in which those life cycles with mergers and splits contribute to 46.3 % of the total anvil areas. It implies that active convective activities and the behaviors of mergers and splits are still the most important for the anvil budget. On

the other hand, the warm short-lived (warmer than 220 K and less than 5 h) simple life cycles still account for a relatively large portion of anvil areas (20.4 %). These warm and fragile core structures are not efficient at producing anvil clouds but are very frequent in observations and thus also lead to an important contribution to the anvil budget.

5 Conclusion

Tropical convection organizations are normally connected complexes of many convective activities. In this work, a novel variable-BT_{11} segment tracking algorithm is established to segment the CCO into OSs for tracking. The tracked motions of OSs are compared against the observational cloud-top winds to examine the rationality of tracking. Strong correlations between the tracked motions and real winds are found, with small differences in the mean speeds ($-1.6\,\mathrm{m\,s^{-1}}$) and angles (0.5°). These results confirm that tracking is appropriate.

Compared with the previous fixed-threshold and variable-BT_{11} tracking algorithms that focus only on the variation in the area, the novel tracking algorithm developed in this work is designed to track the core structure from initiation to dissipation under the background of CCOs and to document the evolution of both the area and BT_{11} structure (i.e., the cold-core and cold-center BT_{11} for indicating the developing and connecting conditions, respectively, and mergers and splits of cold cores). Precipitation and anvil clouds are explicitly associated with unique cold cores, which is helpful for quantifications of precipitation and anvil production from different convective activities. The life cycles are described by the activities of cold cores, e.g., cold-core-peak strength, mergers and splits.

The essential difference between the fixed-threshold and novel variable-BT_{11} tracking algorithms is the selection of tracking targets. The complex organizations of multiple cold cores are very frequent, and isolated convective bodies are rare, particularly for the deep convection of the cold-core BT_{11} from 190–220 K. This implies that most of the targets identified by the fixed BT_{11} threshold are complex organizations, and their segmentation in the variable-BT_{11} tracking algorithm is necessary. Additionally, in fixed-threshold tracking, mergers and splits are caused by many factors: threshold selection, changes in the connecting conditions and activities of cold cores. This makes the final life cycle in fixed-threshold tracking very complicated. In contrast, in the novel variable-BT_{11} tracking algorithm, mergers and splits are related only to activities of cold cores.

Based on the novel variable-BT_{11} tracking algorithm, the convective processes of precipitation and the production of anvil clouds over the tropical western Pacific Ocean are investigated. Interestingly, the accumulated duration, precipitation and anvil cloud amounts produced in the OS life cycles have simple loglinear relationships with the BT_{11} of the
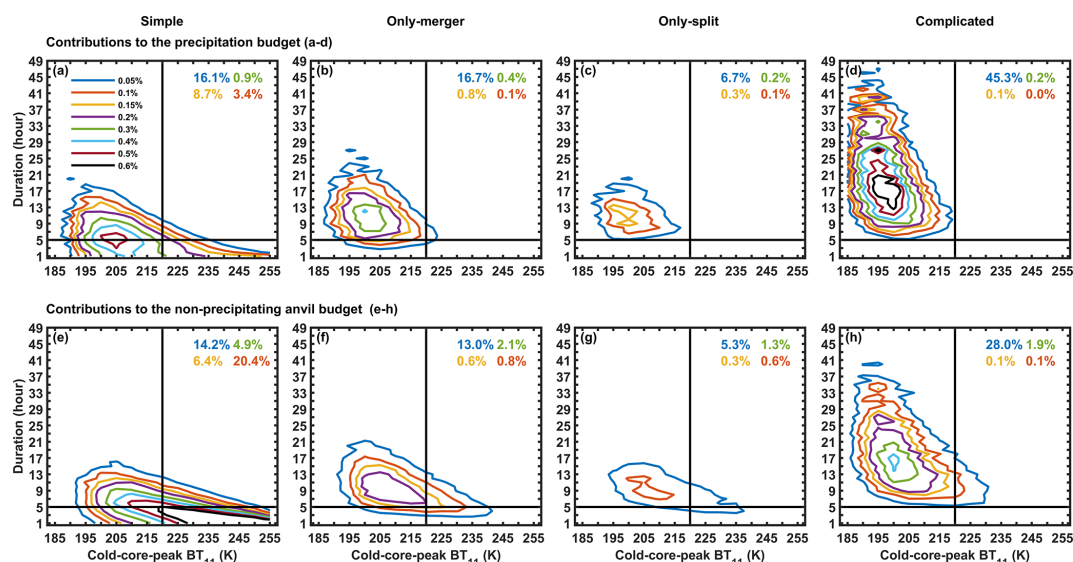
Figure 12. Fractions of the contributions of the OS life cycles of different cold-core-peak BT_{11} values and durations to the total precipitation **(a–d)** and anvil cloud amount **(e–h)** over the tropical western Pacific Ocean, for simple, only-merger, only-split and complicated life cycles, respectively. Two straight black lines for the peak BT_{11} of 220 K and the duration of 5 h are used to discriminate between cold and warm and between long-lived and short-lived life cycles, respectively. In each panel, the fractions of the cold long-lived (blue), warm long-lived (green), cold short-lived (yellow) and warm short-lived (red) contributions are listed in the top right-hand corner.

cold-core peak. During the life cycle, decay takes more time than development does. More precipitation and anvil cloud amounts are also contributed by the decay stage than by the development stage. The difference in the accumulated duration, precipitation and anvil production between the two stages increases exponentially with the decreasing cold-core-peak BT_{11}.

The CCO is the envelope of many convective activities, and it is not expected that all of core structures in CCOs have simple perfect life cycles from convective initiation to anvil dissipation. According to the two modes in the PDFs of durations, those cold structures of the cold-core-peak BT_{11} colder than 220 K and durations greater than 5 h are identified as active convective activities; otherwise, those relatively warm and short-lived structures are secondary weak convective activities.

The occurrence of mergers and splits also strongly relies on the BT_{11} of the cold-core peak, still with a loglinear relationship. Overall, mergers are more frequent than splits in the development stage. In the decay stage, the frequency of mergers and splits shows little difference. But, the frequency of splits in the decay stage is greater than that in the development stage. Lifetime-accumulated precipitation and anvil production are positively related to the occurrence of mergers and splits. For the same cold-core-peak BT_{11}, the increase in lifetime-accumulated precipitation between the simple and complicated life cycles is mostly attributed to the prolonged lifetime. The increase in the lifetime-accumulated anvil cloud amount between the simple and complicated life cycles should be attributed to the increase in both the hourly

anvil production and the prolonged lifetime. The slope of the loglinear relationship between the lifetime-accumulated precipitation or anvil and the cold-core-peak BT_{11} is almost invariant for different types of life cycles.

For the total cloud water budget over the tropical western Pacific Ocean, most of the total precipitation is contributed by long-lived life cycles with the occurrence of mergers and splits, whereas short-lived simple life cycles are less important for precipitation. However, for the anvil cloud amount, the long-lived complicated life cycle and the short-lived simple life cycle are both important.

References

Amidror, I.: Scattered data interpolation methods for electronic imaging systems: a survey, J. Electron. Imaging, 11, 157–176, https://doi.org/10.1117/1.1455013, 2002.

Atlas, R. L., Bretherton, C. S., Sokol, A. B., Blossey, P. N., and Khairoutdinov, M. F.: Tropical Cirrus Are Highly Sensitive to Ice Microphysics Within a Nudged Global Storm-Resolving Model, Geophys. Res. Lett., 51, e2023GL105868, https://doi.org/10.1029/2023GL105868, 2024.

Bao, J. and Sherwood, S. C.: The Role of Convective Self-Aggregation in Extreme Instantaneous Versus Daily Precipitation, J. Adv. Model. Earth Sy., 11, 19–33, https://doi.org/10.1029/2018MS001503, 2019.

Berry, E. and Mace, G. G.: Cloud properties and radiative effects of the Asian summer monsoon derived from A-Train data, J. Geophys. Res.-Atmos., 119, 9492–9508, https://doi.org/10.1002/2014JD021458, 2014.

Blackman, S. S.: Multiple hypothesis tracking for multiple target tracking, IEEE Aero. El. Sys. Mag., 19, 5–18, https://doi.org/10.1109/maes.2004.1263228, 2004.

Blossey, P. N., Bretherton, C. S., and Khairoutdinov, M.: An Energy-Balance Analysis of Deep Convective Self-Aggregation above Uniform SST, J. Atmos. Sci., 62, 4273–4292, https://doi.org/10.1175/jas3614.1, 2005.

Blossey, P. N., Bretherton, C. S., Cetrone, J., and Kharoutdinov, M.: Cloud-Resolving Model Simulations of KWAJEX: Model Sensitivities and Comparisons with Satellite and Radar Observations, J. Atmos. Sci., 64, 1488–1508, https://doi.org/10.1175/jas3982.1, 2007.

Bony, S., Semie, A., Kramer, R. J., Soden, B., Tompkins, A. M., and Emanuel, K. A.: Observed Modulation of the Tropical Radiation Budget by Deep Convective Organization and Lower-Tropospheric Stability, AGU Advances, 1, e2019AV000155, https://doi.org/10.1029/2019av000155, 2020.

Bouniol, D., Roca, R., Fiolleau, T., and Poan, D. E.: Macrophysical, Microphysical, and Radiative Properties of Tropical Mesoscale Convective Systems over Their Life Cycle, J. Climate, 29, 3353–3371, https://doi.org/10.1175/jcli-d-15-0551.1, 2016.

Bresky, W. C., Daniels, J. M., Bailey, A. A., and Wanzong, S. T.: New Methods toward Minimizing the Slow Speed Bias Associated with Atmospheric Motion Vectors, J. Appl. Meteorol. Clim., 51, 2137–2151, https://doi.org/10.1175/jamc-d-11-0234.1, 2012.

Bretherton, C. S.: Insights into low-latitude cloud feedbacks from high-resolution models, Philos. T. Roy. Soc. A, 373, 20140415, https://doi.org/10.1098/rsta.2014.0415, 2015.

Bretherton, C. S., Widmann, M., Dymnikov, V. P., Wallace, J. M., and Bladé, I.: The Effective Number of Spatial Degrees of Freedom of a Time-Varying Field, J. Climate, 12, 1990–2009, https://doi.org/10.1175/1520-0442(1999)012<1990:TENOSD>2.0.CO;2, 1999.

Chen, S. S. and Houze, R. A.: Diurnal variation and lifecycle of deep convective systems over the tropical pacific warm pool, Q. J. Roy. Meteor. Soc., 123, 357–388, https://doi.org/10.1002/qj.49712353806, 1997.

Clement, A. C. and Soden, B.: The Sensitivity of the Tropical-Mean Radiation Budget, J. Climate, 18, 3189–3203, https://doi.org/10.1175/jcli3456.1, 2005.

Coppin, D. and Bony, S.: Physical mechanisms controlling the initiation of convective self-aggregation in a General Circulation Model, J. Adv. Model. Earth Sy., 7, 2060–2078, https://doi.org/10.1002/2015ms000571, 2015.

Daniels, J., Bresky, W., Bailey, A., Allegrino, A., Velden, C. S., and Wanzong, S.: Chapter 8 - Winds from ABI on the GOES-R Series, in: The GOES-R Series, edited by: Goodman, S. J., Schmit, T. J., Daniels, J., and Redmon, R. J., Elsevier, 79–94, https://doi.org/10.1016/B978-0-12-814327-8.00008-1, 2020.

de Laat, A., Defer, E., Delanoë, J., Dezitter, F., Gounou, A., Grandin, A., Guignard, A., Meirink, J. F., Moisselin, J.-M., and Parol, F.: Analysis of geostationary satellite-derived cloud parameters associated with environments with high ice water content, Atmos. Meas. Tech., 10, 1359–1371, https://doi.org/10.5194/amt-10-1359-2017, 2017.

Deng, M., Mace, G. G., and Wang, Z.: Anvil Productivities of Tropical Deep Convective Clusters and Their Regional Differences, J. Atmos. Sci., 73, 3467–3487, https://doi.org/10.1175/jas-d-15-0239.1, 2016.

Doelling, D. R., Loeb, N. G., Keyes, D. F., Nordeen, M. L., Morstad, D., Nguyen, C., Wielicki, B. A., Young, D. F., and Sun, M.: Geostationary Enhanced Temporal Interpolation for CERES Flux Products, J. Atmos. Ocean. Tech., 30, 1072–1090, https://doi.org/10.1175/jtech-d-12-00136.1, 2013.

Doelling, D. R., Sun, M., Nguyen, L. T., Nordeen, M. L., Haney, C. O., Keyes, D. F., and Mlynczak, P. E.: Advances in Geostationary-Derived Longwave Fluxes for the CERES Synoptic (SYN1deg) Product, J. Atmos. Ocean. Tech., 33, 503–521, https://doi.org/10.1175/jtech-d-15-0147.1, 2016.

Feidas, H. and Cartalis, C.: Application of an automated cloud-tracking algorithm on satellite imagery for tracking and monitoring small mesoscale convective cloud systems, Int. J. Remote Sens., 26, 1677–1698, https://doi.org/10.1080/01431160512331338023, 2007.

Feng, Z., Dong, X., Xi, B., Schumacher, C., Minnis, P., and Khaiyer, M.: Top-of-atmosphere radiation budget of convective core/stratiform rain and anvil clouds from deep convective systems, J. Geophys. Res.-Atmos., 116, D23202, https://doi.org/10.1029/2011jd016451, 2011.

Feng, Z., Leung, L. R., Houze, R. A., Hagos, S., Hardin, J., Yang, Q., Han, B., and Fan, J.: Structure and Evolution of Mesoscale Convective Systems: Sensitivity to Cloud Microphysics in Convection-Permitting Simulations Over the United States, J. Adv. Model. Earth Sy., 10, 1470–1494, https://doi.org/10.1029/2018ms001305, 2018.

Feng, Z., Hardin, J., Barnes, H. C., Li, J., Leung, L. R., Varble, A., and Zhang, Z.: PyFLEXTRKR: a flexible feature tracking Python software for convective cloud analysis, Geosci. Model Dev., 16, 2753–2776, https://doi.org/10.5194/gmd-16-2753-2023, 2023.

Fiolleau, T. and Roca, R.: An Algorithm for the Detection and Tracking of Tropical Mesoscale Convective Systems Using Infrared Images From Geostationary Satellite, IEEE T. Geosci. Remote, 51, 4302–4315, https://doi.org/10.1109/tgrs.2012.2227762, 2013.

Fu, R., Del Genio, A. D., and Rossow, W. B.: Behavior of Deep Convective Clouds in the Tropical Pacific Deduced from ISCCP Radiances, J. Climate, 3, 1129–1152, https://doi.org/10.1175/1520-0442(1990)003<1129:Bodcci>2.0.CO;2, 1990.

Fu, Y., Sun, J., Fu, S., Zhang, Y., and Ma, Z.: Initiations of Mesoscale Convective Systems in the Middle Reaches of the Yangtze River Basin Based on FY-4A Satellite Data: Statistical Characteristics and Environmental Conditions, J. Geophys. Res.-Atmos., 128, e2023JD038630, https://doi.org/10.1029/2023jd038630, 2023.

Gasparini, B., Sokol, A. B., Wall, C. J., Hartmann, D. L., and Blossey, P. N.: Diurnal Differences in Tropical Maritime Anvil Cloud Evolution, J. Climate, 35, 1655–1677, https://doi.org/10.1175/jcli-d-21-0211.1, 2022.

Giangrande, S., Clothiaux, E., and Kollias, P.: Active Remote Sensing of CLouds (ARSCL1CLOTH), ARM Data Center [data set], https://doi.org/10.5439/1996113, 1999.

Goyens, C., Lauwaet, D., Schröder, M., Demuzere, M., and Van Lipzig, N. P. M.: Tracking mesoscale convective systems in the Sahel: relation between cloud parameters and precipitation, Int. J. Climatol., 32, 1921–1934, https://doi.org/10.1002/joc.2407, 2011.

Heikenfeld, M., Marinescu, P. J., Christensen, M., Watson-Parris, D., Senf, F., van den Heever, S. C., and Stier, P.: tobac 1.2: towards a flexible framework for tracking and analysis of clouds in diverse datasets, Geosci. Model Dev., 12, 4551–4570, https://doi.org/10.5194/gmd-12-4551-2019, 2019.

Hendon, H. H. and Woodberry, K.: The diurnal cycle of tropical convection, J. Geophys. Res., 98, 16623–16637, https://doi.org/10.1029/93jd00525, 1993.

Hersbach, H., Bell, B., Berrisford, P., Hirahara, S., Horányi, A., Muñoz-Sabater, J., Nicolas, J., Peubey, C., Radu, R., Schepers, D., Simmons, A., Soci, C., Abdalla, S., Abellan, X., Balsamo, G., Bechtold, P., Biavati, G., Bidlot, J., Bonavita, M., Chiara, G., Dahlgren, P., Dee, D., Diamantakis, M., Dragani, R., Flemming, J., Forbes, R., Fuentes, M., Geer, A., Haimberger, L., Healy, S., Hogan, R. J., Hólm, E., Janisková, M., Keeley, S., Laloyaux, P., Lopez, P., Lupu, C., Radnoti, G., Rosnay, P., Rozum, I., Vamborg, F., Villaume, S., and Thépaut, J. N.: The ERA5 global reanalysis, Q. J. Roy. Meteor. Soc., 146, 1999–2049, https://doi.org/10.1002/qj.3803, 2020.

Hollars, S., Fu, Q., Comstock, J., and Ackerman, T.: Comparison of cloud-top height retrievals from ground-based 35 GHz MMCR and GMS-5 satellite observations at ARM TWP Manus site, Atmos. Res., 72, 169-186, https://doi.org/10.1016/j.atmosres.2004.03.015, 2004.

Holloway, C. E., Wing, A. A., Bony, S., Muller, C., Masunaga, H., L'Ecuyer, T. S., Turner, D. D., and Zuidema, P.: Observing Convective Aggregation, Surv. Geophys., 38, 1199–1236, https://doi.org/10.1007/s10712-017-9419-1, 2017.

Houze, R. A.: Mesoscale convective systems, Rev. Geophys., 42, RG4003, https://doi.org/10.1029/2004rg000150, 2004.

Huang, X., Hu, C., Huang, X., Chu, Y., Tseng, Y.-h., Zhang, G. J., and Lin, Y.: A long-term tropical mesoscale convective systems dataset based on a novel objective automatic tracking algorithm, Clim. Dynam., 51, 3145–3159, https://doi.org/10.1007/s00382-018-4071-0, 2018.

Huffman, G. J., Adler, R. F., Arkin, P., Chang, A., Ferraro, R., Gruber, A., Janowiak, J., McNab, A., Rudolf, B., and Schneider, U.: The Global Precipitation Climatology Project (GPCP) Combined Precipitation Dataset, B. Am. Meteorol. Soc., 78, 5–20, https://doi.org/10.1175/1520-0477(1997)078<0005:Tgpcpg>2.0.CO;2, 1997.

Huffman, G. J., Adler, R. F., Bolvin, D. T., Gu, G., Nelkin, E. J., Bowman, K. P., Hong, Y., Stocker, E. F., and Wolff, D. B.: The TRMM Multisatellite Precipitation Analysis (TMPA): Quasi-Global, Multiyear, Combined-Sensor Precipitation Estimates at Fine Scales, J. Hydrometeorol., 8, 38–55, https://doi.org/10.1175/jhm560.1, 2007.

Huffman, G. J., Stocker, E. F., Bolvin, D. T., Nelkin, E. J., and Tan, J.: GPM IMERG Final Precipitation L3 Half Hourly 0.1 degree x 0.1 degree V07, Goddard Earth Sciences Data and Information Services Center (GES DISC) [data set], https://doi.org/10.5067/GPM/IMERG/3B-HH/07, 2023.

Igel, M. R., Drager, A. J., and van den Heever, S. C.: A CloudSat cloud object partitioning technique and assessment and integration of deep convective anvil sensitivities to sea surface temperature, J. Geophys. Res.-Atmos., 119, 10515–10535, https://doi.org/10.1002/2014jd021717, 2014.

Keeler, E., Burk, K., and Kyrouac, J.: Balloon-Borne Sounding System (SONDEWNPN), ARM user facility [data set], https://doi.org/10.5439/1595321, 2001.

Kolios, S. and Feidas, H.: A warm season climatology of mesoscale convective systems in the Mediterranean basin using satellite data, Theor. Appl. Climatol., 102, 29–42, https://doi.org/10.1007/s00704-009-0241-7, 2009.

La, T. V. and Messager, C.: Convective System Observations by LEO and GEO Satellites in Combination, IEEE J. Sel. Top. Appl., 14, 11814–11823, https://doi.org/10.1109/jstars.2021.3127401, 2021.

Laing, A. G., Carbone, R., Levizzani, V., and Tuttle, J.: The propagation and diurnal cycles of deep convection in northern tropical Africa, Q. J. Roy. Meteor. Soc., 134, 93–109, https://doi.org/10.1002/qj.194, 2008.

Leese, J. A., Novak, C. S., and Clark, B. B.: An Automated Technique for Obtaining Cloud Motion from Geosynchronous Satellite Data Using Cross Correlation, J. Appl. Meteorol., 10, 118–132, https://doi.org/10.1175/1520-0450(1971)010<0118:AATFOC>2.0.CO;2, 1971.

Lindzen, R. S., Chou, M.-D., and Hou, A. Y.: Does the Earth Have an Adaptive Infrared Iris?, B. Am. Meteorol. Soc., 82, 417–432, https://doi.org/10.1175/1520-0477(2001)082<0417:Dtehaa>2.3.Co;2, 2001.

Matsui, T., Zeng, X., Tao, W.-K., Masunaga, H., Olson, W. S., and Lang, S.: Evaluation of Long-Term Cloud-Resolving Model Simulations Using Satellite Radiance Observations and Multifrequency Satellite Simulators, J. Atmos. Ocean. Tech., 26, 1261–1274, https://doi.org/10.1175/2008jtecha1168.1, 2009.

Mauritsen, T. and Stevens, B.: Missing iris effect as a possible cause of muted hydrological change and high climate sensitivity in models, Nat. Geosci., 8, 346–351, https://doi.org/10.1038/ngeo2414, 2015.

Merrill, R. T., Menzel, W. P., Baker, W., Lynch, J., and Legg, E.: A Report on the Recent Demonstration of NOAA's Upgraded Capability to Derive Cloud Motion Satellite Winds, B. Am. Meteorol. Soc., 72, 372–376, https://doi.org/10.1175/1520-0477-72.3.372, 1991.

Minnis, P., Trepte, Q. Z., Sun-Mack, S., Chen, Y., Doelling, D. R., Young, D. F., Spangenberg, D. A., Miller, W. F., Wielicki, B. A., Brown, R. R., Gibson, S. C., and Geier, E. B.: Cloud Detection in Nonpolar Regions for CERES Using TRMM VIRS and Terra and Aqua MODIS Data, IEEE T. Geosci. Remote, 46, 3857–3884, https://doi.org/10.1109/TGRS.2008.2001351, 2008.

Minnis, P., Sun-Mack, S., Young, D. F., Heck, P. W., Garber, D. P., Chen, Y., Spangenberg, D. A., Arduini, R. F., Trepte, Q. Z., Smith, W. L., Ayers, J. K., Gibson, S. C., Miller, W. F., Hong, G., Chakrapani, V., Takano, Y., Liou, K.-N., Xie, Y., and Yang, P.: CERES Edition-2 Cloud Property Retrievals Using TRMM VIRS and Terra and Aqua MODIS Data– Part I: Algorithms, IEEE T. Geosci. Remote, 49, 4374–4400, https://doi.org/10.1109/tgrs.2011.2144601, 2011.

Muller, C. and Bony, S.: What favors convective aggregation and why?, Geophys. Res. Lett., 42, 5626–5634, https://doi.org/10.1002/2015GL064260, 2015.

NASA/LARC/SD/ASDC: SatCORPS CERES GEO Edition 4 MTSAT-1R, Version 1.0, NASA Langley Atmospheric Science Data Center DAAC [data set], https://doi.org/10.5067/MTS01/CERES, 2017.

Nieman, S. J., Menzel, W. P., Hayden, C. M., Gray, D., Wanzong, S. T., Velden, C. S., and Daniels, J.: Fully Automated Cloud-Drift Winds in NESDIS Operations, B. Am. Meteorol. Soc., 78, 1121–1133, https://doi.org/10.1175/1520-0477(1997)078<1121:FACDWI>2.0.CO;2, 1997.

Powell, S. W., Houze, R. A., Kumar, A., and McFarlane, S. A.: Comparison of Simulated and Observed Continental Trop-

ical Anvil Clouds and Their Radiative Heating Profiles, J. Atmos. Sci., 69, 2662–2681, https://doi.org/10.1175/jas-d-11-0251.1, 2012.

Rennó, N. O., Emanuel, K. A., and Stone, P. H.: Radiative-convective model with an explicit hydrologic cycle: 1. Formulation and sensitivity to model parameters, J. Geophys. Res.-Atmos., 99, 14429–14441, https://doi.org/10.1029/94jd00020, 1994.

Richards, F. and Arkin, P.: On the Relationship between Satellite-Observed Cloud Cover and Precipitation, Mon. Weather Rev., 109, 1081–1093, https://doi.org/10.1175/1520-0493(1981)109<1081:Otrbso>2.0.CO;2, 1981.

Ruppert, J. H. and Hohenegger, C.: Diurnal Circulation Adjustment and Organized Deep Convection, J. Climate, 31, 4899–4916, https://doi.org/10.1175/jcli-d-17-0693.1, 2018.

Salonen, K. and Bormann, N.: Atmospheric Motion Vector observations in the ECMWF system: Fifth year report, ECMWF, https://doi.org/10.13140/RG.2.1.3767.6404, 2016.

Santek, D., Dworak, R., Nebuda, S., Wanzong, S., Borde, R., Genkova, I., García-Pereda, J., Galante Negri, R., Carranza, M., Nonaka, K., Shimoji, K., Oh, S. M., Lee, B.-I., Chung, S.-R., Daniels, J., and Bresky, W.: 2018 Atmospheric Motion Vector (AMV) Intercomparison Study, Remote Sensing, 11, 2240, https://doi.org/10.3390/rs11192240, 2019.

Schröder, M., König, M., and Schmetz, J.: Deep convection observed by the Spinning Enhanced Visible and Infrared Imager on board Meteosat 8: Spatial distribution and temporal evolution over Africa in summer and winter 2006, J. Geophys. Res.-Atmos., 114, D05109, https://doi.org/10.1029/2008jd010653, 2009.

Sokol, A. B. and Hartmann, D. L.: Tropical Anvil Clouds: Radiative Driving Toward a Preferred State, J. Geophys. Res.-Atmos., 125, e2020JD033107, https://doi.org/10.1029/2020jd033107, 2020.

Sokol, A. B. and Hartmann, D. L.: Congestus Mode Invigoration by Convective Aggregation in Simulations of Radiative-Convective Equilibrium, J. Adv. Model Earth Sy., 14, e2022MS003045, https://doi.org/10.1029/2022MS003045, 2022.

Suzuki, K., Golaz, J. C., and Stephens, G. L.: Evaluating cloud tuning in a climate model with satellite observations, Geophys. Res. Lett., 40, 4464–4468, https://doi.org/10.1002/grl.50874, 2013.

Takahashi, H. and Luo, Z.: Where is the level of neutral buoyancy for deep convection?, Geophys. Res. Lett., 39, L15809, https://doi.org/10.1029/2012GL052638, 2012.

Tian, Y. D., Peters-Lidard, C. D., Eylander, J. B., Joyce, R. J., Huffman, G. J., Adler, R. F., Hsu, K. L., Turk, F. J., Garcia, M., and Zeng, J.: Component analysis of errors in satellite-based precipitation estimates, J. Geophys. Res.-Atmos., 114, D24101, https://doi.org/10.1029/2009JD011949, 2009.

Tobin, I., Roca, R., and Bony, S.: Observational Evidence for Relationships between the Degree of Aggregation of Deep Convection, Water Vapor, Surface Fluxes, and Radiation, J. Climate, 25, 6885–6904, https://doi.org/10.1175/jcli-d-11-00258.1, 2012.

Tsakraklides, G. and Evans, J. L.: Global and regional diurnal variations of organized convection, J. Climate, 16, 1562–1572, https://doi.org/10.1175/1520-0442(2003)016<1562:GARDVO>2.0.CO;2, 2003.

Velden, C. S., Olander, T. L., and Wanzong, S.: The Impact of Multispectral *GOES-8* Wind Information on Atlantic Tropical Cyclone Track Forecasts in 1995. Part I:

Dataset Methodology, Description, and Case Analysis, Mon. Weather Rev., 126, 1202–1218, https://doi.org/10.1175/1520-0493(1998)126<1202:TIOMGW>2.0.CO;2, 1998.

Wall, C. J., Hartmann, D. L., Thieman, M. M., Smith Jr., W. L., and Minnis, P.: The Life Cycle of Anvil Clouds and the Top-of-Atmosphere Radiation Balance over the Tropical West Pacific, J. Climate, 31, 10059–10080, https://doi.org/10.1175/JCLI-D-18-0154.1, 2018.

Williams, M. and Houze Jr., R. A.: Satellite-Observed Characteristics of Winter Monsoon Cloud Clusters, Mon. Weather Rev., 115, 505–519, https://doi.org/10.1175/1520-0493(1987)115<0505:SOCOWM>2.0.CO;2, 1987.

Wing, A. A. and Emanuel, K. A.: Physical mechanisms controlling self-aggregation of convection in idealized numerical modeling simulations, J. Adv. Model. Earth Sy., 6, 59–74, https://doi.org/10.1002/2013ms000269, 2014.

Wing, A. A., Emanuel, K., Holloway, C. E., and Muller, C.: Convective Self-Aggregation in Numerical Simulations: A Review, Surv. Geophys., 38, 1173–1197, https://doi.org/10.1007/s10712-017-9408-4, 2017.

Yang, K., Wang, Z., Deng, M., and Dettmann, B.: Combining CloudSat/CALIPSO and MODIS measurements to reconstruct tropical convective cloud structure, Remote Sens. Environ., 287, 113478, https://doi.org/10.1016/j.rse.2023.113478, 2023.

Yang, R., Zhang, Y., Sun, J., and Li, J.: The comparison of statistical features and synoptic circulations between the eastward-propagating and quasi-stationary MCSs during the warm season around the second-step terrain along the middle reaches of the Yangtze River, Sci. China Earth Sci., 63, 1209–1222, https://doi.org/10.1007/s11430-018-9385-3, 2020.

Yuan, J. and Houze Jr., R. A.: Global Variability of Mesoscale Convective System Anvil Structure from A-Train Satellite Data, J. Climate, 23, 5864–5888, https://doi.org/10.1175/2010jcli3671.1, 2010.

Yuan, J. and Houze Jr., R. A.: Deep Convective Systems Observed by A-Train in the Tropical Indo-Pacific Region Affected by the MJO, J. Atmos. Sci., 70, 465–486, https://doi.org/10.1175/JAS-D-12-057.1, 2013.

Yuan, J., Houze Jr., R. A., and Heymsfield, A. J.: Vertical Structures of Anvil Clouds of Tropical Mesoscale Convective Systems Observed by CloudSat, J. Atmos. Sci., 68, 1653–1674, https://doi.org/10.1175/2011jas3687.1, 2011.

Zhao, M.: An Investigation of the Connections among Convection, Clouds, and Climate Sensitivity in a Global Climate Model, J. Climate, 27, 1845–1862, https://doi.org/10.1175/jcli-d-13-00145.1, 2014.

Zhao, M., Golaz, J. C., Held, I. M., Ramaswamy, V., Lin, S. J., Ming, Y., Ginoux, P., Wyman, B., Donner, L. J., Paynter, D., and Guo, H.: Uncertainty in Model Climate Sensitivity Traced to Representations of Cumulus Precipitation Microphysics, J. Climate, 29, 543–560, https://doi.org/10.1175/jcli-d-15-0191.1, 2016.

Zhao, W., Marchand, R., and Fu, Q.: The diurnal cycle of clouds and precipitation at the ARM SGP site: Cloud radar observations and simulations from the multiscale modeling framework, J. Geophys. Res.-Atmos., 122, 7519–7536, https://doi.org/10.1002/2016jd026353, 2017.

Zinner, T., Mannstein, H., and Tafferner, A.: Cb-TRAM: Tracking and monitoring severe convection from onset over rapid development to mature phase using multi-channel Meteosat-8 SEVIRI data, Meteorol. Atmos. Phys., 101, 191–210, https://doi.org/10.1007/s00703-008-0290-y, 2008.

Zinner, T., Forster, C., de Coning, E., and Betz, H.-D.: Validation of the Meteosat storm detection and nowcasting system Cb-TRAM with lightning network data – Europe and South Africa, Atmos. Meas. Tech., 6, 1567–1583, https://doi.org/10.5194/amt-6-1567-2013, 2013.